Inorganic Chemistry

Article

pubs.acs.org/IC

Charge and Spin States in Schiff Base Metal Complexes with a Disiloxane Unit Exhibiting a Strong Noninnocent Ligand Character: Synthesis, Structure, Spectroelectrochemistry, and Theoretical Calculations

Maria Cazacu,[†] Sergiu Shova,*[,†] Alina Soroceanu,[†] Peter Machata,[‡] Lukas Bucinsky,[‡] Martin Breza,[‡] Peter Rapta,*[,‡] Joshua Telser,[§] J. Krzystek,[∥] and Vladimir B. Arion*[,⊥]

[†]"Petru Poni" Institute of Macromolecular Chemistry, Alea Gr. Ghica Voda 41A, 700487 Iasi, Romania

[‡]Institute of Physical Chemistry and Chemical Physics, Faculty of Chemical and Food Technology, Slovak University of Technology, Radlinského 9, SK-81237 Bratislava, Slovak Republic

[§]Department of Biological, Chemical and Physical Sciences, Roosevelt University, 430 South Michigan Avenue, Chicago, Illinois 60605 United States

[∥]National High Magnetic Field Laboratory, Florida State University, Tallahassee, Florida 32310 United States

[⊥]Faculty of Chemistry, Institute of Inorganic Chemistry, University of Vienna, Währinger Strasse 42, A-1090 Vienna, Austria

Supporting Information

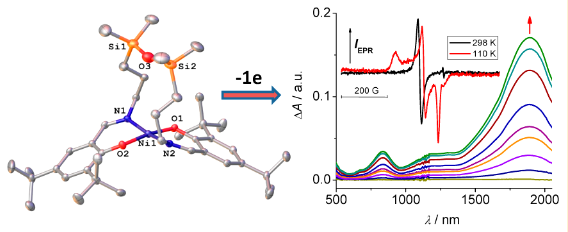

ABSTRACT: Mononuclear nickel(II), copper(II), and manganese(III) complexes with a noninnocent tetradentate Schiff base ligand containing a disiloxane unit were prepared in situ by reaction of 3,5-di-*tert*-butyl-2-hydroxybenzaldehyde with 1,3-bis(3-aminopropyl)-tetramethyldisiloxane followed by addition of the appropriate metal(II) salt. The ligand H_2L resulting from these reactions is a 2:1 condensation product of 3,5-di-*tert*-butyl-2-hydroxybenzaldehyde with 1,3-bis(3-aminopropyl)tetramethyldisiloxane. The resulting metal complexes, $NiL·0.5CH_2Cl_2$, $CuL·1.5H_2O$, and $MnL(OAc)·0.15H_2O$, were characterized by elemental analysis, spectroscopic methods (IR, UV−vis, X-band EPR, HFEPR, ^1H NMR), ESI mass spectrometry, and single crystal X-ray diffraction. Taking into account the well-known strong stabilizing effects of *tert*-butyl groups in positions 3 and 5 of the aromatic ring on phenoxyl radicals, we studied the one-electron and two-electron oxidation of the compounds using both experimental (chiefly spectroelectrochemistry) and computational (DFT) techniques. The calculated spin-density distribution and localized orbitals analysis revealed the oxidation locus and the effect of the electrochemical electron transfer on the molecular structure of the complexes, while time-dependent DFT calculations helped to explain the absorption spectra of the electrochemically generated species. Hyperfine coupling constants, *g*-tensors, and zero-field splitting parameters have been calculated at the DFT level of theory. Finally, the CASSCF approach has been employed to theoretically explore the zero-field splitting of the $S = 2$ MnL(OAc) complex for comparison purposes with the DFT and experimental HFEPR results. It is found that the *D* parameter sign strongly depends on the metal coordination geometry.

INTRODUCTION

Metal complexes with a "noninnocent" ligand exist either as a metal−ligand radical $M^{n+}(L^{\bullet})$ or a higher valent metal complex $M^{(n+1)+}(L^{-})$. Subtle changes of electronic structure could significantly alter the redox site within the complex.[1] In many cases a temperature-dependent equilibrium between these two limiting states exists.[2,3] Structural changes can affect the orbital overlap between the central atom and the ligand also affecting this equilibrium, e.g., in the case of four-coordinate complexes due to a tetrahedral distortion of square-planar coordination geometry. One-electron oxidized salen-type nickel complexes often contain the ligand-radical form $Ni^{2+}(L^{\bullet})$ both in the solid state and in solution, but the coordination environment can shift the redox site to the central atom with Ni(III) complex ($Ni^{3+}(L^{-})$) formation in solution.[4−6] On the other hand, for certain copper salen derivatives the high-valent diamagnetic Cu(III) state ($Cu^{3+}(L^{-})$) dominates in the solid state, while a temperature-dependent equilibrium between $Cu^{3+}(L^{-})$ and $Cu^{2+}(L^{\bullet})$ was suggested to occur in solution.[7] For the Ni(II) complex with a tetradentate ligand based on *S*-methylisothiosemicarbazide, we confirmed the temperature-dependent valence tautomerism between nickel(III)-phenolate species and its nickel(II)-phenoxyl radical counterpart. At room temperature, the $[Ni^{II}(L^{\bullet -})]^{+}$ species dominates, while at 77 K both $[Ni^{II}(L^{\bullet -})]^{+}$ and $[Ni^{III}(L^{2-})]^{+}$ are present in an approximately 1:1 molar ratio.[8]

Received: February 4, 2015
Published: June 1, 2015

DOI: 10.1021/acs.inorgchem.5b00229
Inorg. Chem. 2015, 54, 5691−5706

A large number of bis(phenolate)metal(II) complexes with symmetric salen-type N_2O_2 ligands, prepared by condensation reactions of suitably protected 2-hydroxy-benzaldehydes in positions 3 and 5 with various diamines, reduced salen-type, and other Schiff bases have been reported.[9] Nickel(II), copper(II), and zinc(II) complexes with symmetric salen-type ligands are generally four-coordinate and essentially planar adopting a *cis*-configuration of N_2O_2 donor atoms around the metal ion. Incorporation of space-demanding substituents or spacers between salicylidene moieties with three and more carbon atoms increases the tetrahedral distortion, which is important for stabilizing Cu(I) in this coordination environment. Rare examples of copper(II) complexes with nearly tetrahedral coordination geometries are well-documented in the literature.[10]

Quite recently we discovered that 2-hydroxybenzaldehyde and related derivatives react with 1,3-bis(3-aminopropyl)-tetramethyldisiloxane in the presence of a copper(II) salt in 2:1:1 molar ratio with the formation of tetrahedrally distorted square-planar copper(II) complexes of tetradentate Schiff bases with *trans*-configuration of N_2O_2 donor atoms.[11] The most interesting feature is the formation of a 12-membered central chelate ring including the tetramethyldisiloxane unit, which separates the aliphatic chains, significantly reducing the mechanical strain in the emerging chelate ring. We called this a “shoulder yoke effect” by analogy with the load-spreading ability of such an ancient device. The effect of the disiloxane unit on the Schiff base formation and its coordinating ability was investigated, and the catalytic oxidation properties of these new copper(II) complexes were studied in detail. However, the redox properties and characterization of their oxidation states remain to be clarified. Our preliminary electrochemical measurements on the above-mentioned complexes showed irreversible oxidation in nonaqueous solutions. Therefore, by taking into account the well-known strong stabilizing effect of *tert*-butyl groups in positions 3 and 5 of the aromatic ring on phenoxyl radicals, we prepared new metal complexes with Schiff bases containing a disiloxane unit with substituted phenolic moieties (**1**−**3**) as shown in Scheme 1. For comparison complexes **4**−**6** reported previously[11] were also synthesized.

Scheme 1. Complexes Prepared in This Work

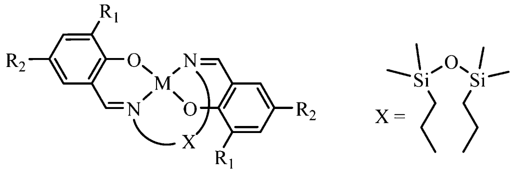

$R_1 = R_2 = {}^tBu$, M = Ni	NiL	(**1**)
$R_1 = R_2 = {}^tBu$, M = Cu	CuL	(**2**)
$R_1 = R_2 = {}^tBu$, M = Mn(OAc)	MnL(OAc)	(**3**)
R_1 = H, $R_2 = NO_2$, M = Cu	CuL^1	(**4**)
$R_1 = R_2$ = Br, M = Cu	CuL^2	(**5**)
R_1 = H, R_2 = Cl, M = Cu	CuL^3	(**6**)

In addition, we performed a detailed spectroelectrochemical and theoretical study of electron transfer in these novel metal complexes. DFT calculations of the optimized ground state geometries, excited states, spin-density distributions, and the localized orbitals analysis are reported to reveal the effect of electrochemical electron transfer on the molecular structure of the complexes, and time-dependent DFT calculations are used to explain the absorption spectra of the electrochemically generated species. EPR parameters such as hyperfine coupling interaction, *g*-tensors, and zero-field splitting (ZFS) were investigated at the DFT level of theory, and the CASSCF approach was employed to compute the ZFS in MnL(OAc).

■ EXPERIMENTAL SECTION

Materials. 3,5-Di-*tert*-butyl-2-hydroxybenzaldehyde was from Aldrich, 99%, mp 59−61 °C. Dichloromethane (CH_2Cl_2, puriss; absolute; $w(H_2O) < 0.001\%$) was purchased from Sigma-Aldrich and used without additional purification. Tetrabutylammonium hexafluorophosphate ($TBAPF_6$) was received from Fluka and dried 24 h at 80 °C in a vacuum oven and stored in a desiccator before use. Decamethylferrocene (DmFc) from Fluka was used as received. Nitrogen gas of technical grade was from Messer production. The copper complexes **4**−**6** were prepared as reported previously.[11]

***NiL·0.5CH$_2$Cl$_2$* (*1·0.5CH$_2$Cl$_2$*).** A solution of 3,5-di-*tert*-butyl-2-hydroxybenzaldehyde (0.5 g, 2.31 mmol) in CH_3OH/CH_2Cl_2 1:1 (6 mL) was added to a solution of 1,3-bis(3-aminopropyl)-tetramethyldisiloxane (0.27 g, 1.07 mmol) in CH_3OH/CH_2Cl_2 1:1 (6 mL). The resulting mixture was heated at 70 °C for 3 h, and then $NiCl_2{\cdot}6H_2O$ (0.29 g, 1.20 mmol) in CH_3OH/CH_2Cl_2 1:1 (6 mL) was added under stirring. The solution was allowed to stand at room temperature. Small crystals of X-ray diffraction quality were separated by filtration after 1 h, washed with methanol, and dried in air. Yield: 0.2 g, 24.0%. Calcd for $C_{40.5}H_{67}ClN_2NiO_3Si_2$ (*M* 780.29 g/mol), %: C, 62.34; H, 8.65; N, 3.59. Found, %: C, 62.21; H, 9.13; N, 3.96. ^1H NMR (500 MHz, $CDCl_3$): δ 12.74 (s, 2H, CH=N), 7.69 (d, *J* = 2.37 Hz, 2H, ArH), 6.94 (d, *J* = 2.37 Hz, 2H, ArH), 6.32 (m, 2H, CH_2N), 5.88 (m, 2H, CH_2N), 4.01 (m, 2H, CH_2N), 1.73 (m, 2H, CH_2Si), 0.71 (m, 2H, CH_2Si), 1.38 (s, 18H, $C(CH_3)_3$), 1.24 (s, 18H, $C(CH_3)_3$), 0.24 (s, 6H, $Si(CH_3)_2$), 0.21 (s, 6H, $Si(CH_3)_2$). IR spectrum (KBr pellet), selected bands, ν_{max}: 2953 s ν(C−H from Si−CH_3), 1620 vs ν(C=N), 1437 m $\nu(CH_2)$, 1255 vs ν(Si−CH_3), 1066 vs ν(Si−O−Si), 839 vs, 785 s ν(Si−CH_3). UV−vis in $CHCl_3$, λ, nm (ε, M^{-1} cm^{-1}): 655 (190), 531 (175), 416 (3950), 398 sh (3638), 333 (7050).

***CuL·1.5H$_2$O* (*2·1.5H$_2$O*).** A solution of 3,5-di-*tert*-butyl-2-hydroxybenzaldehyde (0.5 g, 2.13 mmol) in a mixture of CH_3OH/CH_2Cl_2 1:1 (6 mL) was added to a solution of 1,3-bis(3-aminopropyl)-tetramethyldisiloxane (0.27 g, 1.07 mmol) in CH_3OH/CH_2Cl_2 1:1 (6 mL), and the mixture was heated at 70 °C for 3 h. Then, a solution of $CuCl_2{\cdot}2H_2O$ (0.21 g, 1.21 mmol) in CH_3OH/CH_2Cl_2 1:1 (6 mL) was added under stirring, and the reaction mixture was allowed to stand at room temperature. Small crystals of X-ray diffraction quality were separated by filtration after 30 min, washed with methanol, and dried in air. Yield: 0.4 g, 50.5%. Calcd for $C_{40}H_{69}CuN_2O_{4.5}Si_2$ (*M* 769.70 g/mol), %: C, 62.42; H, 9.04; N, 3.64. Found, %: C, 62.09; H, 8.72; N, 3.76. IR spectrum (ATR), selected bands, ν_{max}: 2954 m, 2911 m ν(C−H from Si−CH_3), 1620 vs ν(C=N), 1436 s $\nu(CH_2)$, 1320 m $\nu(CH_3)$, 1255 s ν(Si−CH_3), 1069 vs ν(Si−O−Si), 791 m ν(Si−CH_3). UV−vis in $CHCl_3$, λ, nm (ε, M^{-1} cm^{-1}): 648 sh (191), 386 sh (8960), 376 (9350), 326 (10 400).

***[MnL(OAc)]·0.15H$_2$O* (*3·0.15H$_2$O*).** A solution of 1,3-bis(3-aminopropyl)tetramethyldisiloxane (0.27 g, 1.07 mmol) in CH_3OH/CH_2Cl_2 1:1 (6 mL) was added under stirring at room temperature to the solution of 3,5-di-*tert*-butyl-2-hydroxybenzaldehyde (0.5 g, 2.13 mmol) in CH_3OH/CH_2Cl_2 1:1 (6 mL). The mixture was stirred at 70 °C for 3 h. Then, the orange solution was added to a solution of $Mn(OAc)_2{\cdot}4H_2O$ (0.29 g, 1.20 mmol) in ethanol (3 mL). The mixture was stirred at room temperature for 10 min. The solution generated prismatic crystals of good quality after 3−4 h on standing at room temperature. These were separated by filtration, washed with methanol, and dried in air. Yield: 0.4 g, 47.1%. Calcd for $C_{42}H_{69.3}MnN_2O_{5.15}Si_2$ (*M* 795.82 g/mol), %: C, 63.39; H, 8.78; N, 3.52. Found, %: C, 63.37; H, 8.87; N, 3.52. IR spectrum (KBr pellet), selected bands, ν_{max}: 2955 m, 2913 m, ν(C−H from Si−CH_3), 1613 s ν(C=N), 1547 s ν(aromatic ring), 1427 s $\nu(CH_2)$, 1387 s $\nu(CH_3)$, 1252 vs ν(Si−CH_3), 1071 vs ν(Si−O−Si), 839 vs ν(Si−CH_3). UV−vis in $CHCl_3$, λ, nm (ε, M^{-1} cm^{-1}): 732 (950), 462 sh (1570), 373 (9700), 318 sh (10 780).

X-ray Crystallography. X-ray diffraction measurements were carried out with an Oxford-Diffraction XCALIBUR E CCD diffractometer equipped with graphite-monochromated Mo Kα radiation. Single crystals were positioned at 40 mm from the detector, and 225, 244, and 271 frames were measured each for 6, 6, and 15 s over 1° scan width for NiL·0.5CH_2Cl_2, CuL·1.5H_2O, and MnL(OAc)·0.15H_2O, respectively. The unit cell determination and data integration were carried out using the CrysAlis package of Oxford Diffraction.[12] All the structures were solved by direct methods using Olex2 software[13] with the SHELXS structure solution program and refined by full-matrix least-squares on F^2 with SHELXL-97.[14] Atomic displacement parameters for non-hydrogen atoms were refined using an anisotropic model. The positional parameters of disordered atoms were refined using available tools (PART, DFIX, and SADI) implemented in SHELXL97, and the combined anisotropic/isotropic refinement has been applied for non-hydrogen atoms. Hydrogen atoms were placed in fixed, idealized positions and refined as riding atoms in the subsequent least-squares model refinements. The molecular plots were obtained using the Olex2 program.[13] The main crystallographic data along with refinement details are summarized in Supporting Information Table S1. CCDC-1046252, -1046251, and -987066 contain supplementary crystallographic data that can be obtained free of charge from The Cambridge Crystallographic Data Centre via www.ccdc.cam.ac.uk/data_request/cif.

Cyclic Voltammetry and EPR/UV–Vis–NIR Spectroelectrochemistry. For cyclic voltammetry studies an Autolab electrochemical analyzer equipped with a PGSTAT 100 potentiostat or a HEKA potentiostat PG 390 were used. Cyclic voltammograms were recorded in CH_2Cl_2 with 0.1 M $TBAPF_6$ as the supporting electrolyte using a one-compartment electrochemical cell with Pt-wire as working electrode, Pt-coil as counter electrode, and Ag-wire pseudoreference electrode. All electrochemical measurements were performed under inert nitrogen or argon atmosphere. DmFc was used as an internal standard. Optical spectra of investigated complexes in dichloromethane were measured by a Shimadzu 3600 UV–vis–NIR spectrometer (Japan). EPR/UV–vis–NIR spectroelectrochemical measurements were carried out in the optical EPR cavity (ER 4104OR, Bruker, Germany) using a custom designed flat EPR cell equipped with a laminated Pt-mesh working electrode, Pt-wire as a counter electrode, and Ag-wire as a pseudoreference electrode. All spectroelectrochemical experiments were carried out in CH_2Cl_2 with 0.2 M $TBAPF_6$ supporting electrolyte. EPR measurements were performed at X-band using a Bruker EMX spectrometer. In situ UV–vis–NIR measurements were performed at Avantes spectrometer AvaSpec-2048x14-USB2 with the CCD detector and AvaSpec-NIR256–2.2 with the InGaAs detector applying the AvaSoft 7.5 software. Halogen and deuterium lamps were used as light sources (AvaLight-DH-S-BAL). Cyclic voltammetry was recorded by potentiostat Heka PG 284 (HEKA Elektronik, Germany). The AvaSpec Avantes and Bruker EMX spectrometers were triggered by potentiostat Heka using the electrochemical software package PotMaster v2x40.

High-Frequency and -Field EPR (HFEPR) Spectroscopy. Low-temperature HFEPR measurements were made using a spectrometer described elsewhere.[15] A variety of forms of MnL(OAc) were used: microcrystalline samples, powder samples immobilized in *n*-eicosane, and frozen solutions (dichloromethane:toluene in an approximately 2:1 proportion). The frozen solution was additionally investigated by X-band EPR using parallel-mode detection in a Bruker Elexsys 680X spectrometer equipped with a dual-mode cavity.

NMR Spectroscopy. The ^1H NMR spectrum of **1** was measured on Bruker Avance III instrument at 500 MHz.

Theoretical Calculations. The geometries of the transition metal complexes NiL, CuL, and MnL(OAc) as well as those of their one- and two-electron oxidized species in the singlet, doublet, triplet, quartet, and/or quintet spin states were optimized at the B3LYP[16,17] level of theory (starting from experimental X-ray diffraction structures) without any symmetry restrictions using the Gaussian03 program package.[18] Singlet spin states of the compounds under study have been treated using an unrestricted formalism ("broken symmetry" treatment). Standard 6-311G* basis sets[19] were used for all atoms. The stability of the obtained structures has been tested by vibrational analysis (no imaginary vibrations). To estimate physical oxidation states of transition metal atoms, their d electron populations (d^x) were evaluated using natural bond orbital (NBO) analysis.[20] Relative energies of various charge and spin states of the same complex have been corrected using restricted open-shell single-point calculations (replacing the electron energy in unrestricted energy data) except "broken symmetry" singlet state (BS) where the energy difference between singlet (E_S) and triplet (E_T) states is evaluated as

$$E_S - E_T = (E_{BS} - E_{uT})/(1 - 0.5\langle S^2\rangle_{BS}) \qquad (1)$$

where E_{uT} is an open-shell energy of the triplet state, and E_{BS} and $\langle S^2\rangle_{BS}$ are the energy and spin-square expectation values of the "broken symmetry" singlet state, respectively.[21,22]

On the basis of the optimized B3LYP geometries, the vertical transition energies and oscillator strengths between the initial and final electron states for electronic absorption spectra were computed by the TD-DFT method. All the basis sets used are included in the Gaussian03 library.[18] Localized orbitals analysis was performed with the ORCA software package[23] using the Pipek–Mezey (PM)[24] method. Canonical orbitals with energies below −1.5 hartree were excluded from the localization procedure. In addition, *g*-tensor,[25] hyperfine coupling constant,[26] and zero-field splitting[27] parameters have been obtained in ORCA, using BLYP and B3LYP levels of theory as well as the conductor-like screening model (COSMO)[28] in CH_2Cl_2 as solvent. The analysis of spatial overlaps between α and β orbitals, which is useful for the identification of the SOMO (single occupied molecular orbital) orbital at the UKS level of theory, has been performed in a local version of TONTO package[29] using the B3LYP/6-311G* wave function from the Gaussian03 fchk file.

The ORCA software package[23] has been used to account for a more rigorous treatment of static electron correction. Complete active space self-consistent field (CASSCF) calculations have been performed for MnL(OAc) species. The CASSCF computations have been carried out to obtain Supporting Information for comparison with DFT based results, i.e., on zero-field splitting in the initial and one-electron oxidized MnL(OAc) species. CASSCF calculations were performed upon a (state averaged) restricted open-shell Hartree–Fock formalism considering only the d-orbitals and d-electrons of the central metal atom. Such an approach has been already successfully applied to numerous high-spin manganese complexes.[27a,c,30,31] The spin–orbit coupling (SOC) contributions to zero-field splitting at the CASSCF level were extended by the spin–spin coupling (SSC) contributions obtained at the multireference configuration interaction (MRCI) level of theory in ORCA and using only the CAS electrons as active. More detail on the usage of CASSCF and post-CASSCF methods can be found in the literature.[27a,c,30,31]

■ RESULTS AND DISCUSSION

Synthesis and Characterization. Complexes NiL·0.5CH_2Cl_2 (**1**·0.5CH_2Cl_2), CuL·1.5H_2O (**2**·1.5H_2O), and [MnL(OAc)]·0.15H_2O (**3**·0.15H_2O), where H_2L is tetradentate Schiff base with a tetramethyldisiloxane unit, have been prepared in situ by condensation reaction of 3,5-di-*tert*-butyl-2-hydroxybenzaldehyde with 1,3-bis(3-aminopropyl)-tetramethyldisiloxane in the presence of three different metal salts, $NiCl_2·6H_2O$, $CuCl_2·2H_2O$, and $Mn(OAc)_2·4H_2O$, in methanol/methylene chloride 1:1 with 24.0, 50.5, and 47.1% yields, respectively. The formation of metal complexes was confirmed by ESI mass spectrometry. In mass spectra registered in positive ion mode the peaks at *m*/*z* 737, 742, and 733 are attributable to $[NiL + H]^+$, $[CuL + H]^+$, and $[MnL]^+$, respectively. Additional peaks at *m*/*z* 759 and 764 in the mass spectra of **1** and **2** were respectively assigned to [NiL + Na]$^+$ and [CuL + Na]$^+$.

X-ray Crystallography. The results of the X-ray crystallography study for **1**−**3** are shown in Figure 1. Selected bond lengths and angles are summarized in Table 1 and Supporting Information Figure S2. There is no cocrystallized solvent in the structure of **2**, while complex **1** crystallizes with dichloromethane in 2:1 molar ratio. The crystal structure of **3** contains only some traces of cocrystallized water. There are three chemically identical, but crystallographically independent molecules (denoted as **A**, **B**, and **C** in Table 1) in the crystal structure of **3**. One crystallographically independent MnL(OAc) complex is depicted in Figure 1c. The structures of **1** and **2** resemble well those of a series of mononuclear complexes with Schiff base ligands based on the 1,3-bis(3-aminopropyl)-tetramethyldisiloxane fragment and substituted 2-hydroxybenzaldehyde (**4**−**6**) that have been reported in our previous work.[11] In both **1** and **2**, the central atom is located in a tetrahedrally distorted square-planar *trans*-N_2O_2 environment. The degree of tetrahedral distortion can be characterized by the parameter τ_4, introduced by Houser, to describe the geometry of four-coordinate metal complexes.[32] The value of τ_4 ranges from 1 for perfect tetrahedral geometry to 0 for an ideal square-planar geometry. This index for complexes **1** and **2** equals 0.142 and 0.374, respectively, which corresponds to a slightly to moderately distorted toward tetrahedral square-planar coordination geometry. Upon coordination of the doubly deprotonated tetradentate ligand L^{2-}, two 6- and one 12-membered chelate rings are formed.

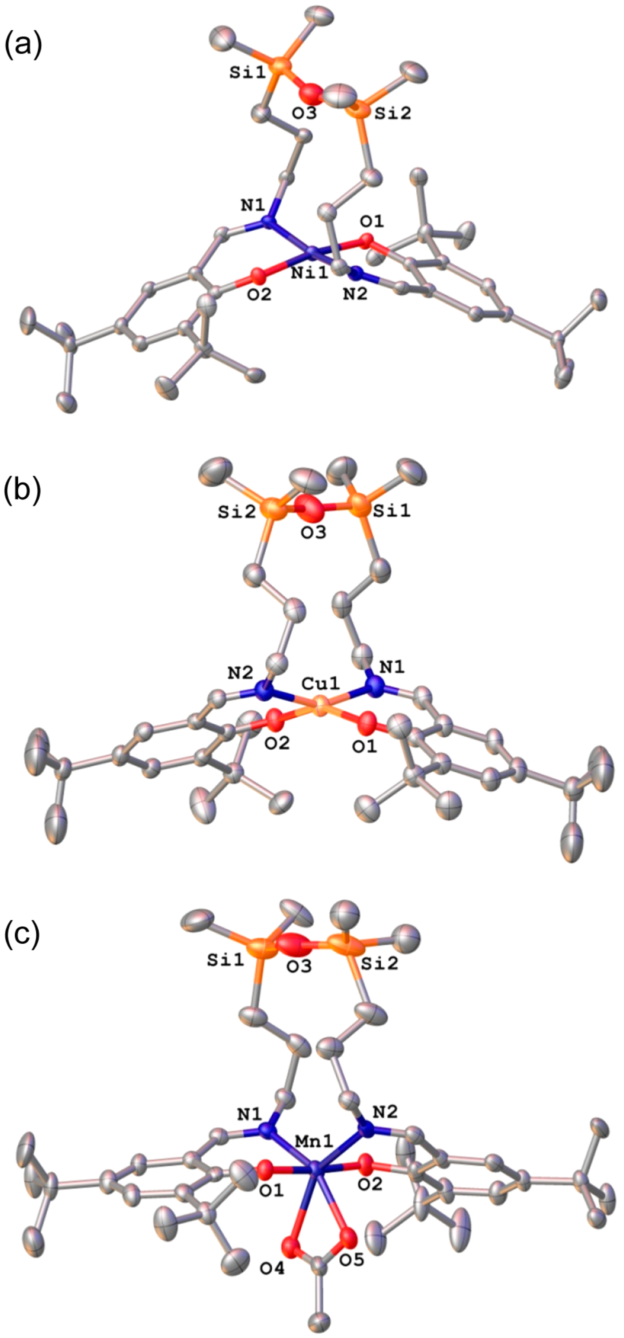

Figure 1. ORTEP views of (a) NiL (**1**), (b) CuL (**2**), and (c) [MnL(OAc)] (**3**), where H_2L is a tetradentate Schiff base with a tetramethyldisiloxane unit, with thermal ellipsoids at 30% probability level. Only one of two disordered positions of *tert*-butyl groups is shown. Hydrogen atoms were omitted for clarity.

Table 1. Coordination Bond Lengths (Å) for NiL·0.5CH$_2$Cl$_2$ (1·0.5CH$_2$Cl$_2$), CuL (2), and MnL(OAc)·0.15H$_2$O (3·0.15H$_2$O)

			3·0.15H$_2$O		
	1·0.5CH$_2$Cl$_2$	2·1.5H$_2$O	A	B	C
M1−N1	1.903(3)	1.963(3)	2.036(5)	2.031(5)	2.069(5)
M1−N2	1.894(3)	1.965(3)	2.105(5)	2.102(5)	2.066(4)
M1−O2	1.849(2)	1.899(2)	1.811(4)	1.827(4)	1.831(4)
M1−O1	1.855(2)	1.913(2)	1.830(4)	1.833(4)	1.833(4)
M1−O4			2.217(4)	2.298(5)	2.128(5)
M1−O5			2.118(5)	2.063(4)	2.203(4)

In contrast to those of **1** and **2**, the first coordination sphere of **3** contains, in addition to the tetradentate ligand L^{2-}, one acetate ion as a bidentate-chelating ligand. Manganese(III) complexes of salen and salpn containing ancillary carboxylate ligands form often polymeric structures in the solid state.[33] A number of mononuclear structures with both unidentate ligation and bidentate-chelating binding of the carboxylates, as for example in [Mn^{III}(3MeO-salen)(OAc)(H$_2$O)] and [Mn(3EtO-salpn)(OAc)]·MeCN, respectively, where 3MeO-salen = dianion of *N,N*′-bis(3-methoxysalicylidene)ethane-1,2-diamine and 3EtO-salpn = dianion of *N,N*′-bis(3-ethoxysalicylidene)propane-1,3-diamine, are also well-documented in the literature.[34] In [Mn(3MeO-salpn)(O$_2$CBu^t)], [Mn(3MeO-salpn)(O$_2$CPr^i)], and [Mn(3EtO-salpn)(OAc)]·MeCN (3EtO-salpn = dianion of *N,N*′-bis(3-ethoxysalicylidene)propane-1,3-diamine), the coordination environment in the equatorial plane consists of three oxygen atoms and one nitrogen, while the axial positions are occupied by oxygen and nitrogen atoms of the tetradentate Schiff base ligand. In **3**, the Mn(III) ion also displays a distorted octahedral geometry with an O_4N_2 donor set. However, in contrast to the literature examples,[34] the equatorial plane in MnL(OAc) is formed by the nitrogen atoms N1 and N2 of the tetradentate ligand and both oxygen atoms (O4 and O5) of the acetate ion, while the axial positions are occupied by the phenolate oxygens O1 and O2. Another feature of note is the observed axial compression in the distorted octahedron. The axial bond lengths Mn−O1 and Mn−O2 at 1.830(4) and 1.811(4) Å are markedly shorter than the equatorial distances Mn−O4, Mn−O5, Mn−N1, and Mn−N2 at 2.217(4), 2.118(5), 2.036(5), and

DOI: 10.1021/acs.inorgchem.5b00229
Inorg. Chem. 2015, 54, 5691−5706

2.105(5) Å, respectively. Distortion of the octahedral coordination geometry is also caused by the coordination of the acetate ligand with the bite angle of 59.32(16)°. This value compares well to 58.21(8)° found in [Mn(3EtO-salpn)(OAc)]·MeCN.[34b] The axial bond angle O1−Mn−O2 is close to linear (175.46(19)°). It should be also noted that in Mn^{III}(*N*-Pr-Sal)$_2$OAc (*N*-Pr-Sal = *N*-propyl-salicylideneamine), where there are no geometrical constraints imposed by a diamine chain as in the present Schiff base complexes, the structure was described as trigonal bipyramidal rather than octahedral because of the lack of a significant Jahn−Teller distortion.[35]

Cyclic Voltammetry. The redox properties of complexes **1**−**3**, as well as, for comparative purposes, of **4**−**6** (see Scheme 1), have been investigated by cyclic voltammetry (CV), at a Pt working electrode in 0.2 M $TBAPF_6/CH_2Cl_2$ solutions, at 25 °C. For **1**, two oxidation waves were observed: the first one is reversible, while the second one shows quasireversible behavior (Figure 2a, green line). A minor anodic peak at around 1.0 V (Figure 2, green line) indicates either the presence of a small impurity in the sample or the follow up product of the one-electron oxidized complex **1** in solution leading to the formation of new redox active species. ^{1}H NMR spectra and spectroelectrochemical studies in combination with ESI mass spectra showed that minor additional signals decreased after chromatographic repurification of the sample and can be presumably attributed to the presence of the free ligand, which also shows a sharp X-band EPR signal upon its oxidation. This signal, however, is very small (less than 2%).

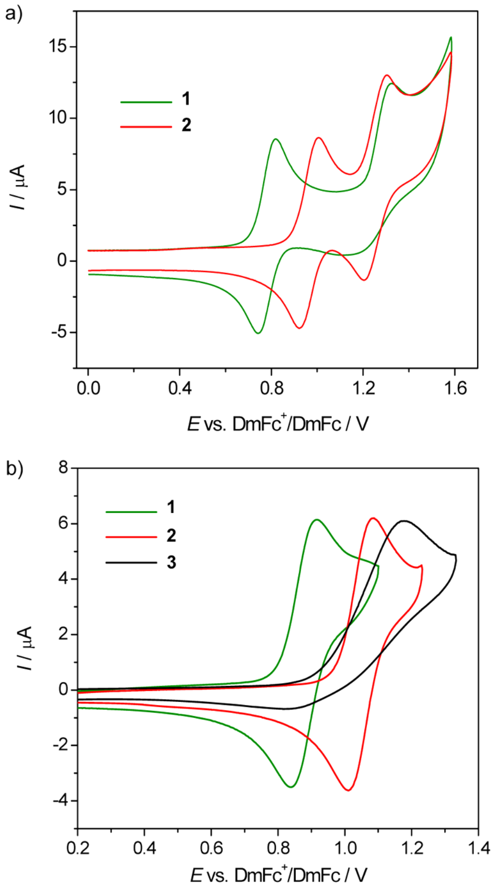

Figure 2. Cyclic voltammograms of (a) **1** and **2** recorded upon anodic oxidation up to the second electron transfer (**1**, green line; **2**, red line) and (b) complexes **1**−**3** in the region of the first anodic peak (**1**, green line; **2**, red line, **3**, black line), all in $TBAPF_6/CH_2Cl_2$ at Pt working electrode (scan rate 100 mV s^{-1}).

Upon oxidation of **2**, two reversible oxidation waves were observed (Figure 2a, red line). In Figure 2b the cyclic voltammograms of complexes **1**−**3** in the region of the first oxidation peak are shown. Complex **1** shows the lowest half-wave oxidation potential with $E_{1/2}$ = +0.87 V versus $DmFc^+$/DmFc as an internal standard. A markedly higher oxidation potential was found for **2** ($E_{1/2}$ = +1.05 V). The half-peak oxidation potential $E_{p/2}$ for **3** is of +1.05 V. In stark contrast to **1** and **2**, the oxidation of **3** is irreversible as shown in Figure 2b (black line). Only a small broad cathodic peak can be observed upon the voltammetric scan reversal. This indicates either a slow electron transfer upon oxidation or irreversible follow up chemical reaction of the oxidized complex **3**. It should be noted that the CV scans of copper(II) complexes **4**−**6** exhibits irreversible behavior in the anodic part (Supporting Information Figure S1a), since they do not contain bulky ^{t}Bu protecting groups in positions 3 and 5 of salicylaldehyde moiety.

On the other hand, some of these complexes show quasireversible redox behavior in the cathodic part as shown in Supporting Information Figure S1b,c. Electrochemical data for the copper(II) complexes **4**−**6** are summarized in Supporting Information Table S2. No reduction was observed for **1**−**3** in the potential window available (Supporting Information Figure S2). Only a very small reduction peak at around −1 V was found for **3**, and we assume that this peak corresponds to a minor impurity and not to the reduction of **3**.

EPR/UV−Vis−NIR spectroelectrochemistry. The optical spectra of complexes **1**−**3** in dichloromethane show two dominating bands in the region from 300 to 500 nm. Additionally, for complex **3** a low-intensity band at 660 nm was observed (Supporting Information Figure S3).

Upon anodic oxidation of **1**, a reversible redox couple in the corresponding cyclic voltammogram at 5 mV s^{-1} was observed (Figure 3a) with a simultaneous evolution of new absorption bands at 835, 1200, and 1894 nm (Figure 3b,c).

Simultaneously, a single-line X-band EPR spectrum was observed with *g*-value of 2.0688 and a line width ΔH_{pp} = 15 G at room temperature (see inset in Figure 3d and Figure 4a, black trace 1).

The EPR signal intensity corresponds well to the above-mentioned optical bands (see Figure 3c,d). The observed EPR line, with *g*-value much higher than that typical for organic radicals (i.e., 2.00), indicates that this signal could be assigned to a predominantly $[Ni(III)L]^+$ species. A spectroelectrochemical experiment coupled with X-band EPR measurement at 130 K allowed observation of the EPR signal of electrochemically oxidized **1** at the first oxidation peak. The rhombic EPR signal with a large *g*-tensor anisotropy (g_1 = 2.1329, g_2 = 2.0553, and g_3 = 2.0183) (Figure 4a, red trace 1) indicates metal-centered oxidation with the formation of a Ni(III) species.[36]

Characteristic Ni(III) EPR signals show obviously large *g* values and large anisotropy due to coupling with the metal nuclear spin, while the organic radical centered species show a *g* value close to 2.00. Recently, for a one-electron oxidized Ni(II) complex with one phenolate group, which was specifically protected by a thiophenyl group in ortho position to the phenolic oxygen, we observed a narrow EPR signal with *g* value of 2.0092 and a line width ΔH_{pp} = 4.7 G at room temperature. This EPR signal can be clearly assigned to a species of predominantly phenoxyl radical character with very little

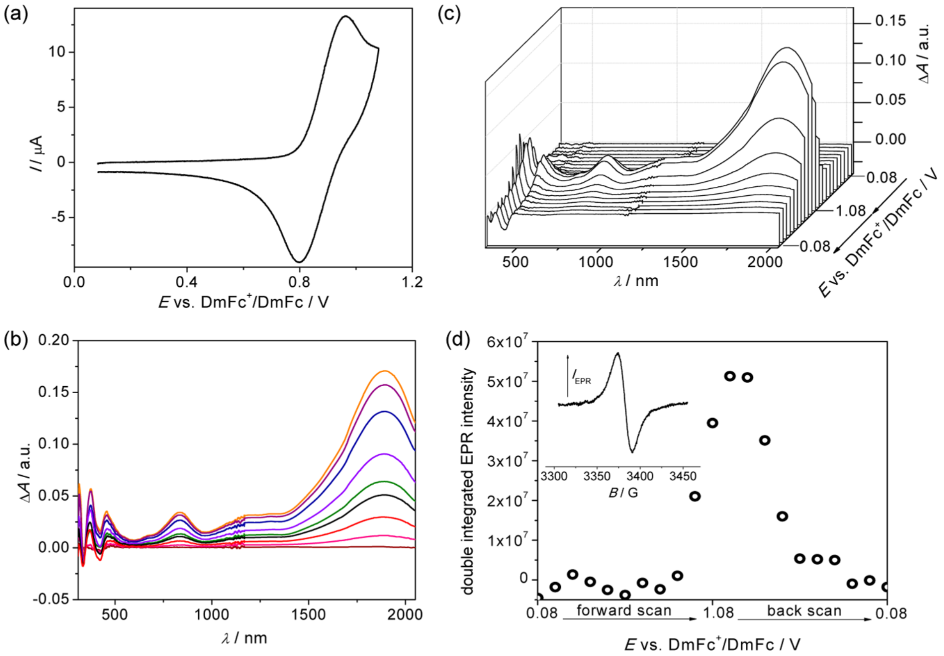

Figure 3. In situ EPR/UV−vis−NIR spectroelectrochemistry of **1** in TBAPF$_6$/CH$_2$Cl$_2$ at the first oxidation peak (Pt-mesh working electrode, scan rate 5 mV s^{-1}). (a) Corresponding cyclic voltammogram, (b) evolution of difference UV−vis−NIR spectra in 2D projection, (c) potential dependence of difference UV−vis−NIR spectra in 3D projection, and (d) potential dependence of double integrated EPR intensity (inset: corresponding room temperature X-band EPR spectrum of [**1**]$^+$).

contribution from the d-orbitals of redox active Ni(II) (see black trace 4 in Figure 4a).[37] This signal becomes only slightly anisotropic with a rhombic pattern at low temperatures (see red trace 4 in Figure 4a) indicating a small contribution of Ni(II) with its more than half-filled 3d^8 configuration. On the other hand, for the one-electron oxidized Ni(II) complex with a single phenolic moiety, suitably protected by bulky *tert*-butyl groups in the 3,5-positions of the parent phenol, we observed anisotropic EPR spectra from two different species with different *g* values at low temperatures (see red trace 3 in Figure 4a), in contrast to the single isotropic narrow EPR signal ($S = {}^1/_2$) measured at room temperature (see black trace 3 in Figure 4a).[8] At room temperature, the *g* value of 2.014 is slightly higher than that for the complex with a thiophenyl group in position 3 of phenolic moiety, and this EPR signal is more anisotropic at 110 K. This indicates the formation of a ligand-centered radical upon one-electron oxidation but with slightly more pronounced delocalization of the unpaired spin onto orbitals of the nickel ion. The new EPR signal, which appeared at 110 K with a large anisotropy ($g_1 = 2.252$, $g_2 = 2.212$, $g_3 = 2.03$) was attributed to a Ni(III) species confirming a temperature-driven tautomerism between nickel(III)-phenolate and nickel(II)-phenoxyl radical states. Consequently, the red trace (3) in Figure 4a clearly illustrates the characteristic features of both nickel(III)-phenolate and nickel(II)-phenoxyl radical states. Interestingly, the EPR signal found for the one-electron species [**1**]$^+$ studied in the present work exhibits features between these two limiting cases (see traces 1 in Figure 4a). Species [**1**]$^+$ shows a broad isotropic EPR signal at a much higher *g*-value of 2.069 (see black trace 3 in Figure 4a) in comparison to the solely ligand-centered radicals. A large anisotropy of the EPR signal at 130 K suggests that the contribution of the central nickel ion is significant. In addition, this EPR signal is very similar to those observed for Ni(III) complexes with dithiolate ligands both at room and low temperatures as illustrated by lines 2 in Figure 4a.[38] The recent results of the X-ray diffraction analysis of (MePh$_3$P)[M(bdt)$_2$] (M = Cu, Ni, Co, bdt = benzene-1,2-dithiolate) showed that the M−S bond lengths are shorter than the reported values for M(II) complexes, providing further evidence that the formal oxidation state of the metal in previously mentioned dithiolate structures is +3.[39] However, the dithiolate ligands are severely noninnocent, and the distribution of the electron density between the central atom and the ligand is more complex making it difficult to determine the physical/formal oxidation state of the central atom. Other recently reported formally Ni(III) systems exhibit EPR spectra that are neither typical Ni(III) nor organic radical in character.[40] Consequently, in a comparison of all EPR spectra shown in Figure 4a we can conclude that the one-electron oxidized species [**1**]$^+$ clearly represents a system with a substantially noninnocent character of the ligand.

In contrast to the straightforward message from EPR experiments, the near-infrared (NIR) bands of the corresponding species discussed above are more complex and are different for each oxidized Ni complex as shown in Figure 4b. Absorption bands in the NIR region for the one-electron oxidized nickel(II)-salen type complexes in CH$_2$Cl$_2$ are mostly attributed to intervalence charge transfer (IVCT) transitions which are ligand-centered, rather than metal-centered.[41] The degree of radical delocalization and classification of the systems can be inferred from a quantitative analysis of absorption bands.[6a] Addition of exogenous monodentate ligands, e.g., pyridine, or use of coordinating solvents such as methanol or DMF, results in formation of six-coordinate nickel(III)-phenolate complexes accompanied by disappearance of the NIR charge-transfer bands.[5a] Taking into account detailed EPR studies discussed above, [**1**]$^+$ can be formulated as a ligand radical with a significant delocalization of the unpaired electron onto the orbitals of the nickel atom. The DFT calculations (see

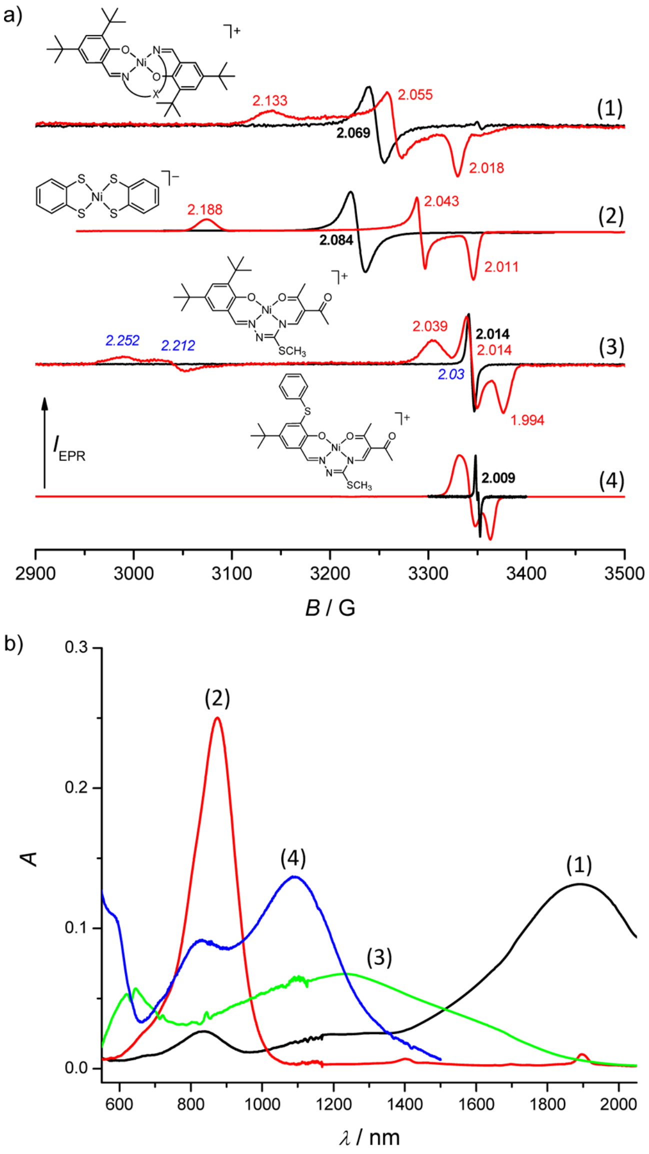

Figure 4. (a) X-band EPR spectra of selected nickel complexes (see line drawings in the figure) in TBAPF$_6$/CH$_2$Cl$_2$ measured at 295 K (black traces) and 110−130 K (red traces) as well as (b) their corresponding NIR spectra.

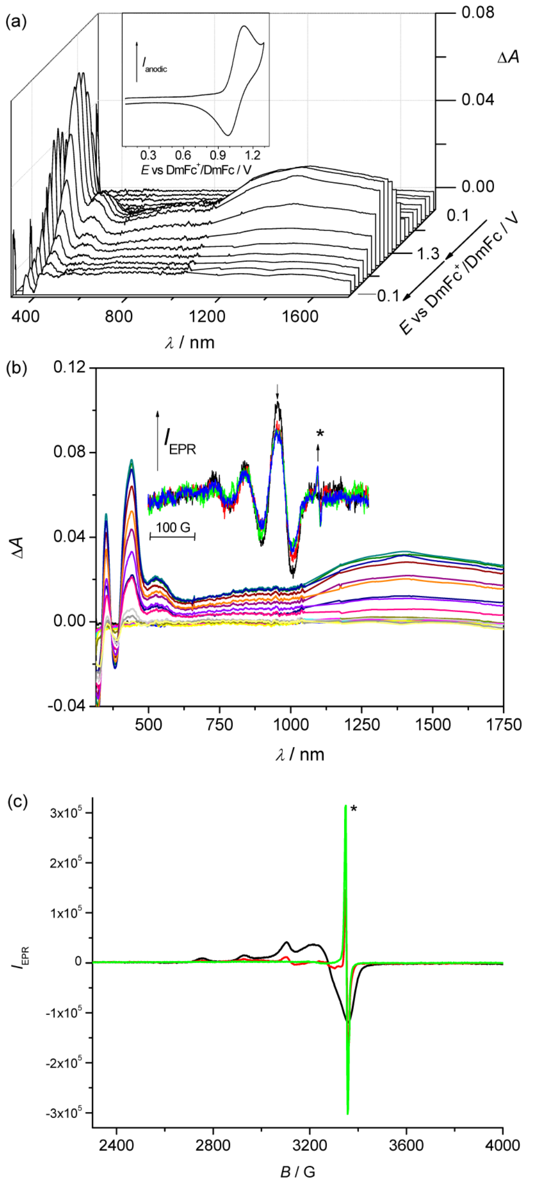

Figure 5. In situ EPR/UV−vis−NIR spectroelectrochemistry of **2** in TBAPF$_6$/CH$_2$Cl$_2$ at the first oxidation peak (Pt-mesh working electrode, scan rate 5 mV s^{-1}). (a) Potential dependence of difference UV−vis−NIR spectra with the corresponding cyclic voltammogram and (b) the evolution of difference UV−vis−NIR spectra in 2D projection. (Inset: EPR spectra measured in situ during oxidation of **2** at the first voltammetric peak (1.2 V) using a large Pt mesh electrode.) (c) EPR spectra of **2** in CH$_2$Cl$_2$ + TBAPF$_6$ measured at 110 K before exhaustive electrolysis (black line), after oxidation of about 80% of **2** (red line) and after nearly 100% oxidation of **2** (green line) at the first oxidation peak.

theoretical part below) show that the intense NIR band at 1894 nm is mainly due to charge transfer from the phenolic groups to the central atom and [NiN$_2$O$_2$] coordination polyhedron.

Upon anodic oxidation of **2**, a reversible voltammetric peak was observed at a scan rate of 5 mV s^{-1} (inset in Figure 5a) with a simultaneous evolution of new optical absorption bands at 530, 895, and 1430 nm (Figure 5a). A slight decrease of the characteristic Cu(II) room temperature EPR signal was also seen. A decrease of this signal was more obvious when using a large Pt mesh working electrode (inset in Figure 5b). An additional electrochemical and X-band EPR experiment using exhaustive electrolysis of **2** in TBAPF$_6$/CH$_2$Cl$_2$ in the region of the first cyclic voltammetric peak was performed. Figure 5c shows EPR spectra of **2** in CH$_2$Cl$_2$ + TBAPF$_6$ measured before exhaustive electrolysis (black trace), after oxidation of about 80% of the complex (red trace) and after one-electron oxidation of the whole sample in the anodic compartment of the coulometric cell (green trace), all measured at 110 K. After complete one-electron oxidation of **2** the characteristic low-temperature Cu(II) EPR signal fully disappears. No EPR signal characteristic of a triplet state of [**2**]$^+$ was observed at 110 K in the X-band region. However, it should be noted that phenoxyl radicals of salen type copper complexes are often EPR silent even in the temperature range 4−100 K, which may be due to their large zero-field splitting parameters. As discussed in the literature,[41b] the EPR silence does not distinguish among antiferromagnetism, ferromagnetism, or diamagnetism of the corresponding radical-copper(II) complex; however, DFT calculations often predict the ferromagnetic S = 1 ground state due to orthogonality between radical and copper d orbitals.

Additionally, as seen for **1**, we observed a narrow EPR signal typical for an organic radical ($g \sim 2.00$) after prolonged electrolysis of **2** at the first anodic peak (see EPR signals marked with an asterisk in Figure 5). The double integral of this signal represents only 2% of the EPR intensity of the Cu(II) signal measured before electrolysis. As already noted for **1**, this signal can be presumably attributed to the minor free ligand impurity leading to the formation of new paramagnetic species.

Manganese(III) in **3** resulted from oxidation of manganese(II) acetate starting material upon reaction with the tetradentate siloxane based ligand generated in situ in the presence of air oxygen. After exhaustive electrolysis of **3** in the region of the first irreversible oxidation peak, no X-band EPR signal was observed indicating a low stability of the oxidized manganese complex, $^{m}[\mathbf{3}]^{+}$, in agreement with the strong irreversibility of the corresponding redox wave.

HFEPR Spectroscopy. Complexes of manganese(III) have been extensively and very successfully investigated by HFEPR spectroscopy, to the extent that such species have been referred to as "the deliciae" of HFEPR and that they "invariably yield good quality spectra".[42] Complex **3** would thus appear to be a perfect candidate for HFEPR investigation. The reality, however, turned out to be different and more complicated, as summarized below.

When investigated as a polycrystalline solid, the complex did produce strong HFEPR spectra at low temperatures (10 K). The spectra (not shown), however, evidently indicated a partial orientation (torquing) of crystallites in the magnetic field, which rendered them uninterpretable. To prevent this orientation, the sample was ground, and the resulting powder fixed into a pellet with *n*-eicosane. The HFEPR spectra of such a pellet (also not shown), however, turned out to be even less useful than those of the loose solid. Specifically, some of the turning points exhibited immense line width, on which there were superimposed imperfections in the powder distribution of the microcrystallites. No spectral analysis of these results was possible. The situation was partly remedied by studying the sample **3** in a low-temperature glass consisting of dichloromethane (DCM):toluene (ca. 2:1 v/v). Certain turning points remained very broad and undefined; however, it was possible to obtain an estimate for the spin Hamiltonian parameters as follows:

$$S = 2,\ D = +3.35\ \mathrm{cm}^{-1},\ E = +0.24\ \mathrm{cm}^{-1}$$
$$(E/D \cong 0.07),\ g = 2.00$$

In the absence of single crystal data, there is no way to determine the sign of E; therefore, using a standard convention that we (and others) have employed in numerous papers, we arbitrarily assign to E the same sign as D, as done, e.g., in Aromí et al.[43]

Figure 6a shows an EPR spectrum of **3** as a glass collected at 10 K and 208 GHz together with two simulations: one corresponding to a negative, the other to a positive value of D.

Although the agreement of the simulations and experiment is at best moderate, the lack of resonances in the high-field region (>8 T) of the experimental spectrum clearly points at the positive D.

Given that even a frozen glass sometimes does not provide ideal powder-pattern HFEPR spectra, we used our standard procedure of tunable-frequency EPR[44] to determine the spin

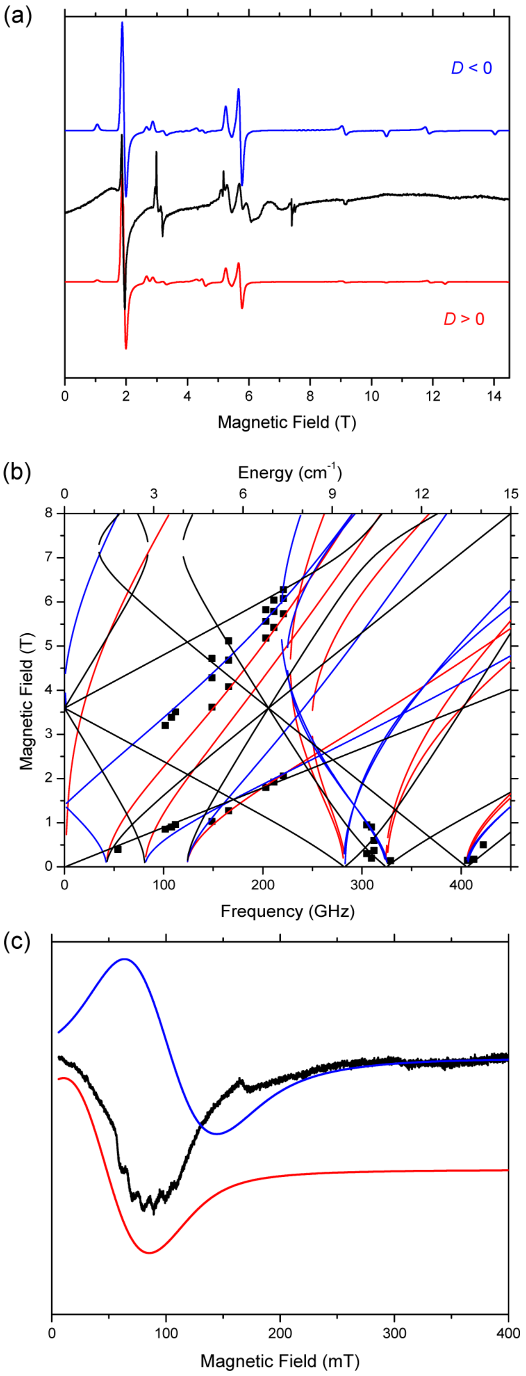

Figure 6. (a) HFEPR spectrum of **3** in a DCM−toluene glass at 10 K and 208 GHz (black trace) and its simulations using spin Hamiltonian parameters as in the text. Blue trace: negative D. Red trace: positive D. The sharp resonances at ca. 3 and 5.2 T are due to adventitious solid dioxygen while the group of equally sharp lines near 7.5 T are ubiquitous $g \cong 2$ impurities. (b) 2-D field/frequency map of turning points in **3** in a DCM−toluene glass at 10 K. Squares: experimental points. Curves simulated with the following $S = 2$ spin Hamiltonian parameters: $|D| = 3.36(5)$ cm^{-1}, $|E| = 0.24(2)$ cm^{-1}, $g_x = g_y = 2.00(1)$, $g_z = 1.99(1)$. Red curves: canonical turning points with $B_0 \| x$; blue curves, $B_0 \| y$; black curves, $B_0 \| z$. (c) An X-band (9.41 GHz) spectrum of **3** in DCM−toluene glass at 15 K using a parallel-mode detection (black trace), together with simulations: the blue trace uses spin Hamiltonian parameters as obtained from the HFEPR experiment; the red trace uses the same parameters with the addition of the fourth-rank zero-field splitting parameter B_4^4 of 98 × 10^{-4} cm^{-1}.

Table 2. $\langle S^2 \rangle$ Expectation Value, Corrected Relative Energy Data of the Optimized Structures under Study (Energy Data Related to Neutral Complexes in the Lowest Spin State), Central Atom d-Electron Populations (d^x), and Number of Localized Orbitals (d_{LOC})

system	$\langle S^2 \rangle$	DFT energy [eV]	free energy at 298 K [eV]	d^x	d_{LOC}
$^1[\mathbf{1}]^0$	0.1169^a	0.0000^a (0.0002^b)	0.0000^a	8.47^a	$4\alpha + 4\beta^a$
$^3[\mathbf{1}]^0$	2.0070	0.0595	−0.0824	8.25	$5\alpha + 3\beta$
$^2[\mathbf{1}]^+$	0.7665	6.1361	6.1199	8.41	$4\alpha + 3.75\beta$
$^4[\mathbf{1}]^+$	3.7709	6.4607	6.2707	8.23	
$^1[\mathbf{1}]^{2+}$	1.1100^a	16.9098	16.8804	8.44	$5\alpha + 3\beta$
$^3[\mathbf{1}]^{2+}$	2.9842	18.7541	18.5656	8.24	$5\alpha + 3\beta$
$^5[\mathbf{1}]^{2+}$	6.0335	17.0239	16.7936	8.23	$5\alpha + 3\beta$
$^2[\mathbf{2}]^0$	0.7528	0.0000	0.0000	9.25	$5\alpha + 4\beta$
$^1[\mathbf{2}]^+$	0.1559^a	6.7540	6.8368	9.26	$5\alpha + 4\beta$
$^3[\mathbf{2}]^+$	2.0177	6.3180	6.2682	9.24	$5\alpha + 4\beta$
$^2[\mathbf{2}]^{2+}$	1.7759	20.1220	20.0742	9.24	
$^4[\mathbf{2}]^{2+}$	3.7837	16.5228	16.4727	9.25	$5\alpha + 4\beta$
$^1[\mathbf{3}]^0$	1.0381^a	0.0000	0.0000	5.19	
$^3[\mathbf{3}]^0$	2.0268	−1.8180	−1.8308	5.17	
$^5[\mathbf{3}]^0$	6.0492	−2.3245	−2.4783	4.93	$4\alpha + 0\beta$
$^2[\mathbf{3}]^+$	1.6616	6.4910	6.4457	5.18	
$^4[\mathbf{3}]^+$	3.8224	4.0390	4.0338	5.01	$3\alpha + 0\beta$

[a] "Broken symmetry" treatment. [b] Restricted treatment of the singlet state.

Hamiltonian parameters, rather than fitting them to single-frequency spectra such as those shown in Figure 6a. The results were collected in a 2-D data set of fields versus frequency, shown in Figure 6b. We cannot offer a ready explanation of the low quality of HFEPR spectra, but have noticed a correlation of that quality with the positive D in multiple Mn(III) complexes, which remain unpublished precisely because of that problem. Romain et al. were likewise unable to observe HFEPR from a bona fide (i.e., tetragonally compressed, but not rhombically distorted) N6 donor set Mn(III) complex.[31] Apparently, the "deliciae of HFEPR spectroscopists" is applicable only to the $D < 0$ case.

An $S = 2$ system with a finite rhombicity factor E/D produces a nominally forbidden $\Delta M_S = 4$ transition at low frequencies and magnetic fields, which is enhanced when using a parallel-mode detection.[45] Due to its biological relevance, the majority of parallel-mode EPR studies on $S = 2$ systems have focused on high-spin Fe(II); however, there have been a number of such studies on high-spin Mn(III). The pioneering work was performed mainly by R. D. Britt and co-workers,[46−51] including biological systems such as MnSOD[47] and Photosystem II.[49] However, there have been several significant, more recent, parallel-mode EPR studies on high-spin Mn(III) coordination complexes: with an octahedral O6 donor set,[52] with a trigonal bipyramidal $N3N_{ax}O_{ax}$ donor set,[53] on *trans*-$[MnF_2(salen)]^-$,[54] on $[MnF_6]^{3-}$,[55] and on porphyrins.[56] Inspired by these works, we performed an X-band experiment using a dual-mode resonator on the same DCM−toluene glass used for the HFEPR experiment. The resulting spectrum is shown in Figure 6c. The X-band spectrum shows a poorly resolved sextet of hyperfine lines due to the $I = {}^5/_2$ nuclear spin (100% abundance) of the ^{55}Mn nucleus, which we did not try to simulate. However, the position of the resonance cannot be reproduced even approximately using the spin Hamiltonian parameters as obtained from HFEPR, with the difference in spectral position between experiment and simulation (blue trace) amounting to ca. 60 mT. A much more successful simulation (red trace) requires addition of a fourth-rank zero-field splitting parameter,. $B_4^4 = +98 \times 10^{-4}$ cm^{-1}, to the second-rank zero-field splitting parameters (D, E) as obtained from HFEPR. (Conversely, adding B_4^4 has very little effect on the position of HFEPR resonances, as shown in Supporting Information Figure S7.) Alternatively, the X-band experiment can be reproduced using a much higher rhombicity factor than that obtained from HFEPR, on the order of $E/D \cong 0.17$, and no fourth-rank ZFS parameters. Such a high rhombicity factor is, however, impossible to reconcile with the HFEPR spectra, and we thus have to assume that B_4^4 is indeed necessary to be included in the spin Hamiltonian.

As is the case with ^{55}Mn(III) hyperfine coupling (see below), there is very little data with which to make any kinds of meaningful comparisons of the fourth-rank zfs parameters. The only examples are the studies by some of us on a complex with a *trans*-N_2O_4 donor set,[43] and that by Krivokapic et al.[42] on the hexaaqua complex. The N_2O_4 complex gave a maximum magnitude fourth-order zero-field splitting parameter, $B_4^4 = +48 \times 10^{-4}$ cm^{-1}, and for the aqua complex, $B_4{}^4 = -58 \times 10^{-4}$ cm^{-1}. In contrast to many other HFEPR studies on Mn(III) (see citations below and in our review articles),[57,58] the data quality here are insufficient to make any extensive discussion.

Analysis of the low-field signal indicates that the ^{55}Mn hyperfine coupling is $A(^{55}\mathrm{Mn})_z = 260(5)$ MHz. No conclusion as to the other hyperfine coupling tensor components can be made, and the assignment to z assumes that the hyperfine and zero-field splitting tensors are collinear. Little information on ^{55}Mn hyperfine coupling in Mn(III) complexes is available, but notable are the HFEPR studies[42] on single crystals of $[Mn(H_2O)_6]^{3+}$ doped into a diamagnetic host where the values $A(^{55}\mathrm{Mn})_{x,y} = -0.0087(2)$ cm^{-1} (261 MHz) and $A(^{55}\mathrm{Mn})_z = -0.005\,31(5)$ cm^{-1} (159.2 MHz) were found. The correspondence between $A(^{55}\ \mathrm{Mn})_z$ seen here and $A(^{55}\ \mathrm{Mn})_{x,y}$ seen for the hexaaqua ion may be coincidental, or may indicate that the hyperfine coupling observed may be $A(^{55}\ \mathrm{Mn})_{x,y}$ due to a mutual rotation of the nuclear and electronic coordinate systems.

DOI: 10.1021/acs.inorgchem.5b00229
Inorg. Chem. 2015, 54, 5691−5706

The positive axial zero-field splitting for Mn(III) in MnL(OAc) is not merely a spectroscopic inconvenience. It is directly related to the structure of the complex. In most cases of six-coordinate Mn(III) ($t_2^3e^1$ in strong field notation), as exemplified by the solution (and most crystal structures; see supporting information of ref 57) of Mn(acac)$_3$,[51] the Jahn−Teller effect in Mn(III) leads to an axial elongation. Ligand-field theory (LFT) predicts that the resulting axial zero-field splitting should be negative, $D < 0$, absent complications from heavy atom ligands such as iodide which exhibits a large SOC, and in the one examined case happens to contribute to the ZFS opposite in sign to that from Mn(III).[59] This negative D value is the case for many examples, as summarized elsewhere.[60] However, as seen in Table 2, the O1−Mn−O2 axis, i.e., the phenolato ligand axis, is compressed: the Mn−O1 distance is 1.832 Å, and the Mn−O2 distance is 1.823 Å, while the Mn−O4 distance is 2.214 Å, that for Mn−O5 is 2.128 Å, that for Mn−N1 is 2.045 Å, and that for Mn−N2 is 2.091 Å (average of molecules **A**, **B**, **C** for all). Thus, there are four Mn−L bonds that are longer than 2.04 Å, and two *trans* bonds that are shorter than 1.84 Å: a clear case of axial compression for a pseudo-octahedral complex. In agreement with LFT, the D value for MnL(OAc) is positive. The theory of the Jahn−Teller effect in HS d^4 systems was extensively developed by the late P. L. W. Tregenna-Piggott,[61,62] and is beyond the scope of this study.

Theoretical Calculations. B3LYP/6-311G* calculations of ${}^{m}[\mathbf{N}]^{q}$ complexes, where m is the spin multiplicity (defined using their spin S as $m = 2S + 1$), q is the total charge, and **N** denotes the studied species (equal to **1**, **2**, or **3**), were performed to produce data such as their free energy values at 298 K (G_{298}). These energies determine their relative stability at room temperature, and total DFT energies (E_{DFT}), which are close to corresponding free energies at very low temperatures (Table 2 and Supporting Information Table S2).

The optimized geometry of the metal coordination polyhedron significantly depends on its spin state. Nevertheless, in the case of transition metal complexes (or in general) it might be often troublesome to compare the optimized geometries directly with the experimental structure data due to solid state effects (see Table 1, Table 3, and Supporting Information Tables S2 and S4). Here especially, the optimized geometry (the coordination polyhedron) of ${}^{5}[\mathbf{3}]^{0}$ is considerably distorted in comparison with the experimental structure. On the other hand, the optimized structure of ${}^{2}[\mathbf{2}]^{0}$ agrees well with the experimental one, and the singlet ${}^{1}[\mathbf{1}]^{0}$ optimized geometry is closer to the experimental structure than that of the triplet ${}^{3}[\mathbf{1}]^{0}$. Following the obtained energetics of the optimized geometries, our DFT calculations (see Table 2) indicate that neutral spin triplet ${}^{3}[\mathbf{1}]^{0}$ complex is more stable at room temperature whereas its singlet spin state counterpart ${}^{1}[\mathbf{1}]^{0}$ is more stable at low temperatures. Note that the energy differences between ${}^{1}[\mathbf{1}]^{0}$ and ${}^{3}[\mathbf{1}]^{0}$ states are only 5.7 kJ mol^{-1} at the DFT level, and −7.9 kJ mol^{-1} for ΔG_{298}, so that solid state effects could be effective. To explore the effects of static electron correlation on the ground state configuration of the initial $[\mathbf{1}]^{0}$ complex, additional (8,5) CASSCF calculations have been performed. These yielded a triplet state as energetically more preferred. In the case of individual state averaged CASSCF calculations the triplet state is 145.7 kJ mol^{-1} (1.510 eV) lower in energy than the singlet state. Even if spanning the CI triplet state expansions with the singlet-state state-specific CASSCF eigenvectors, the triplet ground state is 26.5 kJ mol^{-1} (0.275 eV) below the singlet ground state. The presence of ${}^{1}[\mathbf{1}]^{0}$ and ${}^{3}[\mathbf{1}]^{0}$ species in solution at room temperature will be further discussed via the comparison of the calculated TD-DFT transitions of the two spin states with the measured UV−vis spectrum of ${}^{m}[\mathbf{1}]^{0}$. In addition, a ${}^{m}[\mathbf{1}]^{0}$ compound might be a further instance of the dependence of the preferred spin state (high-spin vs low-spin) on the choice of a DFT functional and/or the amount of exact exchange in the particular functional.[63] For the chosen method, the cationic ${}^{m}[\mathbf{1}]^{+}$ species is more stable in the lower spin state (${}^{2}[\mathbf{1}]^{+}$), whereas the dication prefers the singlet spin state at lower temperatures only, i.e., ${}^{0}[\mathbf{1}]^{2+}$. Cationic ${}^{m}[\mathbf{2}]^{+}$ and dicationic ${}^{m}[\mathbf{2}]^{2+}$ as well as all ${}^{m}[\mathbf{3}]^{q}$ complexes (irrespective of their global charge) prefer the highest spin states.

Table 3. Selected M−N and M−O bond lengths (Å) of $[\mathbf{1}]^{0}$, $[\mathbf{2}]^{0}$, $[\mathbf{3}]^{0}$, $[\mathbf{1}]^{+}$, $[\mathbf{2}]^{+}$, and $[\mathbf{3}]^{+}$ Obtained by DFT Geometry Optimization

	${}^{1}[\mathbf{1}]^{0}$	${}^{3}[\mathbf{1}]^{0}$	${}^{2}[\mathbf{2}]^{0}$	${}^{1}[\mathbf{3}]^{0}$	${}^{3}[\mathbf{3}]^{0}$	${}^{5}[\mathbf{3}]^{0}$
M−N1	1.910	1.986	1.977	2.026	2.027	2.221
M−N2	1.910	1.986	1.977	2.017	2.017	2.074
M−O1	1.872	1.919	1.941	1.892	1.895	1.893
M−O2	1.872	1.919	1.941	1.893	1.893	1.889
M−O4				2.018	2.022	1.995
M−O5				2.037	2.031	2.414
	${}^{2}[\mathbf{1}]^{+}$	${}^{1}[\mathbf{2}]^{+}$	${}^{3}[\mathbf{2}]^{+}$	${}^{2}[\mathbf{3}]^{+}$	${}^{4}[\mathbf{3}]^{+}$	
M−N1	1.905	1.950	1.967	2.038	1.859	
M−N2	1.905	1.950	1.967	2.004	1.858	
M−O1	1.834	1.881	1.943	1.929	1.981	
M−O2	1.834	1.881	1.943	1.848	1.986	
M−O4				1.995	1.992	
M−O5				2.007	1.995	

The physical oxidation state of the first row transition metals (which can significantly differ from their formal oxidation states) might be derived from their d-orbital population d^{x}. Nevertheless, alternative theoretical treatments are desirable. It can be seen that the d-electron populations of central atoms in our systems (Table 2) depend more on the spin state of the complex than on its charge, although these variations are rather small. Consequently, following the changes of the total d-populations of the central atoms allows one to conclude that the redox processes are localized prevailingly on the ligands, in agreement with their "noninnocent" character.

To explore more quantitatively the electronic structure of the central atom in light of crystal field theory and/or formal d-electron configuration, the localized orbitals (d$_{\mathrm{LOC}}$) are worth employing (see Table 2). Another useful option would be the comparison of individual d-populations of atomic orbitals on the central atom.[64,38] Nevertheless, the coordination polyhedra of the studied complexes are not symmetric and hence are less useful for a proper analysis of nonbonding and σ-bonding participating orbitals at the central atoms. As can be seen in Table 2, the d-electron configuration of the central Ni atom changes from d^{8} to d$^{7.75}$ after oxidation of **1**, implying the formation of an intermediate Ni(II)/Ni(III) species in ${}^{2}[\mathbf{1}]^{+}$ as already discussed in the literature[40] and indicated in our EPR study (see Figure 4). The open shell in ${}^{2}[\mathbf{1}]^{+}$ has both ligand-centered and central-atom-centered character, as suggested by the 7.75 d$_{\mathrm{LOC}}$ population and 0.22 spin population on Ni atom, all pointing toward a strong "noninnocent" metal−ligand interaction. In addition, bond lengths in the coordination polyhedron of the optimized structure of $^{2}[\mathbf{1}]^{+}$ are closer to $^{1}[\mathbf{1}]^{0}$ than to $^{3}[\mathbf{1}]^{0}$ which may indicate that the electronic structure in $^{2}[\mathbf{1}]^{+}$ is closer to the neutral singlet species than to the triplet species (see Table 3). The formal d-population in $[\mathbf{1}]^{2+}$ species is found again to be d^{8} for every considered spin state. In the case of restricted Kohn−Sham calculation of $^{1}[\mathbf{1}]^{2+}$, the closed shell $4\alpha + 4\beta$ d^{8} localization is preferred (not shown in Table 2), while in the BS unrestricted Kohn−Sham calculation the $5\alpha + 3\beta$ d^{8} localization scheme remains preferred for the central Ni atom. On the other hand, oxidation of $^{2}[\mathbf{2}]^{0}$ to energetically preferred $^{3}[\mathbf{2}]^{+}$ does not change the formal d-electron configuration of the central copper atom: it remains Cu(II). Thus, following the unchanged number of localized d-orbitals at the central atom, this oxidation is ligand-centered with spin density localized on both the central atom and the ligand. This is also supported by the mutual orthogonality of the $d_{x^2\text{-}y^2}$ orbital of copper with the π-systems of the ligand, which disfavors electron pair formation and leads to preference of the triplet over the singlet state as discussed elsewhere.[41b] Similarly, oxidation to $[\mathbf{2}]^{2+}$ does not affect the formal d^{9}-electron configuration of the central atom. The formal oxidation state of the central atom in $^{5}[\mathbf{3}]^{0}$ can be assigned to Mn(III) following the number of d-orbitals localized on the central atom, consistent with the HFEPR results. The computations indicate that the oxidation state of singly oxidized **3**, i.e., $^{4}[\mathbf{3}]^{+}$, is Mn(IV), electron configuration d^{3}, with spin quartet ground state. Unfortunately, $^{4}[\mathbf{3}]^{+}$ is not long-lived enough to be observable by EPR.

In order to further explore the electronic structure of the species present in solution, TD-DFT calculated transitions were compared to the measured UV−vis transitions. For nickel complex $^{1}[\mathbf{1}]^{0}$, the first computed transition with significant oscillator strength, at 397 nm, corresponds to that from α,β-HOMO to α,β-LUMO where α- and β-HOMO orbitals (from the "broken symmetry" calculation) are almost the same (Supporting Information Figure S4).

The α- and β-HOMO orbitals of $^{1}[\mathbf{1}]^{0}$ are mostly located on the $[NiN_2O_2]$ coordination polyhedron (especially Ni(II) d-orbitals) and on both phenolic moieties. The LUMOs are located similarly. Consequently, the first transition in $^{1}[\mathbf{1}]^{0}$ can be attributed to a transition within the phenolic rings and the remaining part of the tetradentate ligand (except the siloxane bridge and ^{t}Bu groups) and to a high extent also within the metal d-orbitals. Interestingly, the d-orbitals change from out-of-plane (d_{xz}) to in-plane ($d_{x^2-y^2}$) ones. The shape of HOMOs should indicate the oxidation locus on the $[NiN_2O_2]$ coordination polyhedron and both phenolic moieties (Supporting Information Figure S4). The next most intense transition, at 347 nm, corresponds to α,β-HOMO − 1 → α,β-LUMO + 1 and is primarily associated with charge transfer from the phenolic groups to the central atom and $[MN_2O_2]$ coordination polyhedron. It should be noted that two dominating theoretical transitions in the visible region were also found for triplet $^{3}[\mathbf{1}]^{0}$ state (red columns in Figure 7). The calculated lowest energy electron transition in the most stable mono-oxidized nickel complex $^{2}[\mathbf{1}]^{+}$ at 1610 nm (0.7704 eV) can be attributed to β-HOMO → β-LUMO and very well correlates with the experimentally observed intense NIR absorption upon anodic oxidation of **1**.

This transition is partially accompanied by charge transfer from the phenolic groups to the central atom and $[MN_2O_2]$ coordination polyhedron (Figure 7). Spin density calculated for the most stable monocharged doublet state $^{2}[\mathbf{1}]^{+}$ is predominantly located on both phenolic moieties and the $[NiN_2O_2]$ coordination polyhedron (including out-of-plane Ni d-orbitals) confirming strong "noninnocence" of the ligand (Figure 8a).

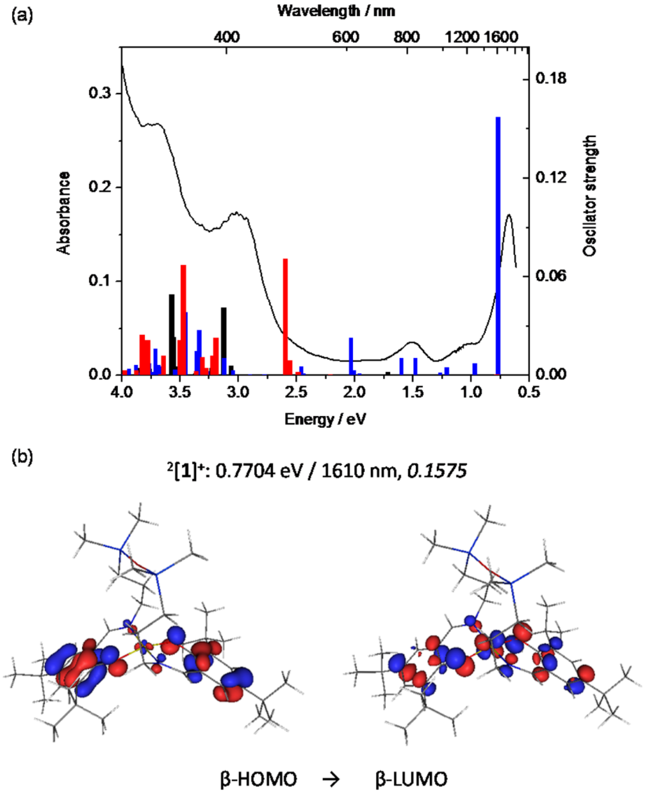

Figure 7. (a) Comparison of the experimental absorption spectrum for one-electron-oxidized nickel complex **1** (black trace) with calculated transitions for $^{1}[\mathbf{1}]^{0}$ (black columns), $^{3}[\mathbf{1}]^{0}$ (red columns), and monocharged $^{2}[\mathbf{1}]^{+}$ (blue columns). (b) B3LYP orbitals contributing dominantly to the lowest calculated (TD-B3LYP) electronic transition for $^{2}[\mathbf{1}]^{+}$; the value in italics is the oscillator strength.

Note that a ligand-to-ligand charge transfer has been already reported for a nonsymmetric Ni complex with O,N donor atoms in the *cis* position[6a,41a] (the asymmetric ligand has one bridging carbon atom in sp^{2} and the other sp^{3} hybridization), being an example of the class III mixed-valence complexes. In addition, the spin density of $^{2}[\mathbf{1}]^{+}$ has a shape very similar to that of the α-HOMO of $^{2}[\mathbf{1}]^{+}$, i.e., α-HOMO represents the singly occupied molecular orbital (SOMO). In addition, α-HOMO of $^{2}[\mathbf{1}]^{+}$ has the largest spatial overlap with the particular β-LUMO, where β-LUMO orbital can be associated with the singly unoccupied MO (SUMO). Thus, the open shell for $^{2}[\mathbf{1}]^{+}$ can be straightforwardly assigned either to α-HOMO (as SOMO) or to β-LUMO (as SUMO).

For the paramagnetic copper complex $^{2}[\mathbf{2}]^{0}$, the most intense calculated transition at 339 nm (3.6627 eV) corresponds to β-HOMO − 4 → β-LUMO, and α-HOMO → α-LUMO + 1, and indicates the charge transfer from the phenolic groups to the central atom and $[MN_2O_2]$ coordination polyhedron (Supporting Information Figure S6). Analogously, the contributions of β-HOMO → β-LUMO and β-HOMO − 9 → β-LUMO excitations to the low-energy transitions at 442 nm (2.8078 eV) indicate the charge transfer from ligands to CuO_2N_2 coordination polyhedron. Note that the shape of β-LUMO in $^{2}[\mathbf{2}]^{0}$ represents the SOMO in the classical MO representation, which is furthermore confirmed by its overlap presumably with

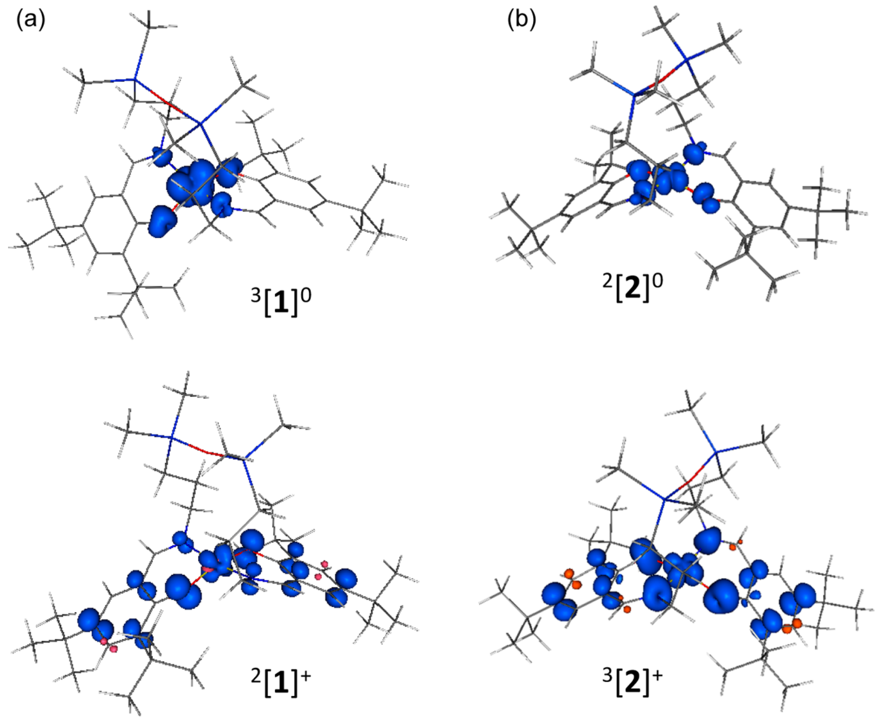

Figure 8. (a) Spin density at ±0.005 au (e/bohr^3) level for the neutral Ni complex **1** in calculated triplet ^{3}[**1**]^0 state and for monocharged ^{2}[**1**]$^+$ doublet state (blue, α spin; red, β spin density). (b) Spin density at ±0.005 au (e/bohr^3) level for selected redox states of copper complex **2** (blue, α spin; red, β spin density).

α-HOMO − 2 (which is 70% when considering the square of the overlap of β-LUMO with α-HOMO − 2; α-HOMO has exactly the same shape as β-HOMO and thus cannot represent the SOMO). Moreover, most of the unrestricted DFT spin-density distribution in ^{2}[**2**]^0 very well correlates with the β-LUMO. Thus, the theoretical spin-density distribution in ^{2}[**2**]^0 is located mainly on in-plane d(Cu) orbitals and adjacent coordinated N_2O_2 atoms (Figure 8b). In agreement with the found number of localized d-orbitals on the central atom which does not change during the oxidation of ^{2}[**2**]^0, the redox active site for oxidation should be mainly located on the phenolic rings, i.e., on the ligand-centered α-HOMO.

In the case of copper complex **2**, the lowest energy electron transition at 1352 nm (0.9173 eV) observed for the singlet state of the ^{1}[**2**]$^+$ cation (see red columns in Figure 9a) very well correlates with the experimentally observed NIR band. As for ^{2}[**1**]$^+$, this band is attributed to the α,β-HOMO to α,β-LUMO transitions, with dominating charge transfer from the phenolic groups to the central atom and [MN_2O_2] coordination polyhedron (Figure 9b). This correlates well with NIR absorption and theoretical studies of [Cu(**Sal**)]SbF_6 (**Sal** = *N*,*N*′-bis(3,5-di-*tert*-butylsalicylidene)-1,2-cyclohexane-(1*R*,2*R*)-diamine)),, where the NIR bands were attributed to ligand-to-metal charge transfer (LMCT) bands as the TD-DFT HOMOs were mainly ligand-centered, while there is a higher contribution of the copper d orbital to the LUMO.[7] In addition, it was shown that the LMCT band intensity at 18 000 cm^{-1} (555 nm) was temperature-dependent indicating valence tautomerism between Cu(III)-phenolate and Cu(II)-phenoxyl radical.

The TD-B3LYP transitions of ^{1}[**2**]$^+$ in the UV−vis region fit the experimental spectra less well than those of ^{3}[**2**]$^+$. On the other hand, the energetically preferred triplet state ^{3}[**2**]$^+$ has its NIR transition shifted to well below the experimentally

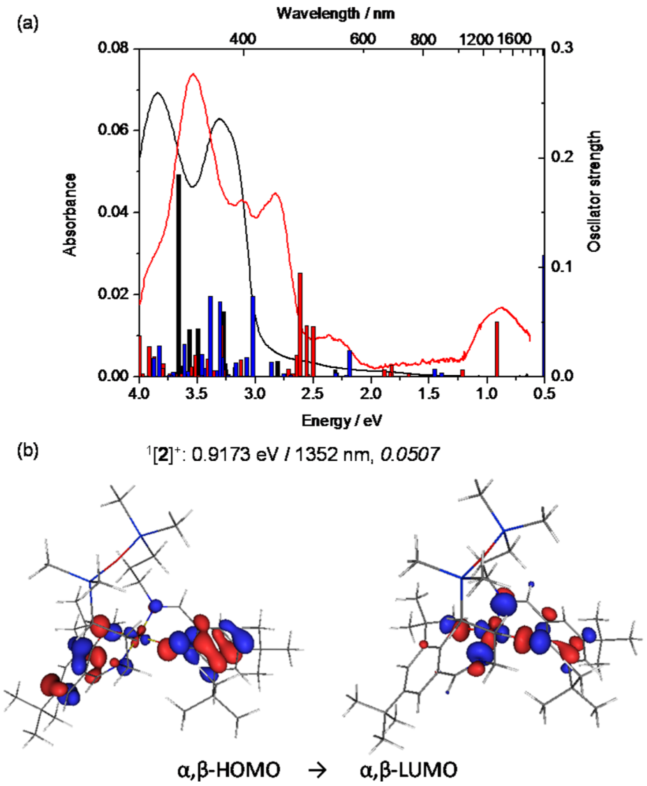

Figure 9. (a) Comparison of the experimental absorption spectra for neutral (black trace) and one-electron-oxidized (red trace) copper complex **2**, and calculated electronic transitions for ^{2}[**2**]^0 (black columns), ^{1}[**2**]$^+$ (red columns), and ^{3}[**2**]$^+$ (blue columns). (b) B3LYP orbitals contributing to the lowest TD-B3LYP electron transition for ^{1}[**2**]$^+$. The value in italics is the oscillator strength.

observed NIR band (see blue columns in Figure 9a). Overall, the experimental spectrum of $\mathbf{2}^+$ seems to be described by the TD-B3LYP transitions of both species (triplet and singlet) equally well. Hence, for the oxidized species $[\mathbf{2}]^+$ one can conclude from only the energetics (total DFT energy and/or free energy at 298 K) that the triplet state should be preferred. However, this conclusion is also supported by (and closely related to) the orthogonality and/or small/unfavorable overlap between $d_{x^2-y^2}$ of Cu and the π-systems of the ligands.[41b]

It should be noted that the concept of "broken-symmetry" diradicals for a singlet state is not universally accepted by the chemical community. Nevertheless, its reality has been clearly demonstrated, e.g., in the simplest case, by that of dinuclear "paddle-wheel" complexes.[65] Despite the "broken-symmetry" wave function being not fully correct, its qualitative features should be very useful for describing electronic structure. Transition metal complexes can contain corresponding α- and β-spin orbitals with significantly different spatial properties, which diverge in parallel with their energy difference.[21] This implies the possibility of a different distribution of α- and β-electrons over the complex, even in the singlet spin state.

The calculated spin-density distribution pattern in $^3[\mathbf{2}]^+$ has significant spin population on both phenolic moieties and strong spin delocalization over a coordination polyhedron including the central atom. In EPR spectroelectrochemical experiments a decrease of the EPR signal from Cu(II) species was confirmed upon anodic oxidation of **2** at the first oxidation peak (see Figure 5b,c).

For manganese complex **3**, electronic transitions were calculated for the singlet $^1[\mathbf{3}]^0$, triplet $^3[\mathbf{3}]^0$, and quintet $^5[\mathbf{3}]^0$ states as shown in Figure 10a. As expected, the optimal fit of the experimental spectrum was found for the energetically most favored quintet state $^5[\mathbf{3}]^0$.

For complex $^5[\mathbf{3}]^0$, the first computed electronic transition with significant oscillator strength, at 808 nm (1.8312 eV), corresponds to α-HOMO → α-LUMO. The next intense electronic transition was calculated at 677 nm (1.5349 eV) and corresponds to α-HOMO − 2 → α-LUMO. In both cases a strong charge transfer from phenolic moieties to the central Mn atom and the corresponding coordination polyhedron is evident (Supporting Information Figure S6).

Formally, the spin-density distribution in all three spin states (singlet, triplet, quintet) is located mainly on the central Mn atom with the highest unpaired spin density for $^5[\mathbf{3}]^0$ as shown in Figure 10. This correlates well with our HFEPR measurements for **3**.

Finally, the calculated EPR parameters, g-tensor, zero-field splitting (D, E values), and hyperfine coupling constants (HFCCs), of open-shell systems $^2[\mathbf{1}]^+$, $^3[\mathbf{2}]^+$, $^3[\mathbf{1}]^0$, $^2[\mathbf{2}]^0$, $^4[\mathbf{3}]^+$, and $^5[\mathbf{3}]^0$, are briefly compared to available experimental data, where the DFT results are compiled in Supporting Information Table S5 and the zero-field splitting parameters of $^5[\mathbf{3}]^0$ and $^4[\mathbf{3}]^+$ are quoted in Table 4.[66] It is found that the g-tensor values of $^2[\mathbf{1}]^+$ ($g_1 = 2.091$, $g_2 = 2.047$, $g_3 = 2.005$, $g_{iso} = 2.048$) yield at the B3LYP/6-311G*/COSMO(CH_2Cl_2) level of theory reasonable agreement with experiment. The B3LYP/6-311G* g-tensor value of $^5[\mathbf{3}]^0$ (1.99) agrees well with the experimentally determined value, while the B3LYP/6-311G* value of A_z hyperfine coupling value is underestimated by almost 50% in comparison to experiment when using the B3LYP/6-311G* reoptimized geometry (for the experimental X-ray diffraction structure **C** the calculated A_z value is underestimated by only 25%).

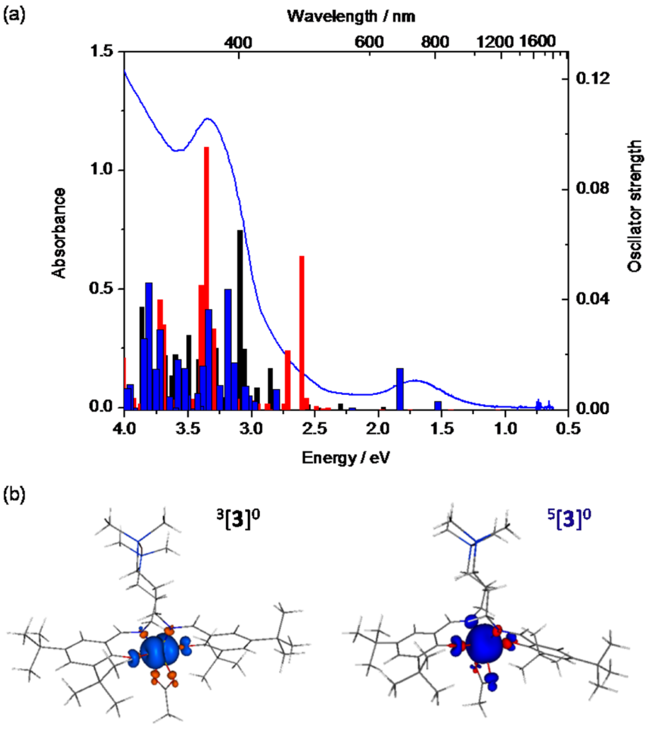

Figure 10. (a) Experimental absorption spectrum for Mn complex **3** (blue trace) and calculated electronic transitions for $^1[\mathbf{3}]^0$ (red columns), $^3[\mathbf{3}]^0$ (black columns), and $^5[\mathbf{3}]^0$ (blue columns) spin states of the neutral complex. (b) Spin density at ±0.005 au (e/bohr^3) level for the neutral Mn complex **3** in triplet $^3[\mathbf{3}]^0$ and quintet $^5[\mathbf{3}]^0$ spin states (blue, α spin; red, β spin density).

Table 4. Zero-Field Splitting Parameters of $^5[\mathbf{3}]^0$ and $^4[\mathbf{3}]^+$ with 6-311G* Basis Set Used (All Values in cm^{-1})

system	method	details[a]	contribution	D	$\lvert E/D \rvert$
$^5[\mathbf{3}]^0$	BLYP[b]		SOC + SSC	−1.580	0.223
	BLYP[b]		SOC	−1.247	0.228
	CAS(4,5)[b]	5/5 + 3/35	SOC + SSC	−3.317	0.231
	CAS(4,5)[b]	5/5 + 3/35	SOC	−2.839	0.234
$^5[\mathbf{3}]^0$	BLYP[c]		SOC + SSC	+1.813	0.058
	BLYP[c]		SOC	+1.487	0.054
	CAS(4,5)[c]	5/5 + 3/35	SOC + SSC	+3.546	0.077
	CAS(4,5)[c]	5/5 + 3/35	SOC	+2.996	0.074
$^4[\mathbf{3}]^+$	BLYP		SOC + SSC	−0.569	0.110
	BLYP		SOC	−0.434	0.102
	CAS(3,5)	4/10 + 2/30	SSC + SOC	−0.769	0.088
	CAS(3,5)	4/10 + 2/30	SOC	−0.633	0.075

[a] m/s means multiplicities (m) over number of states(s) employed in the state average. [b] Theoretical (T), B3LYP/6-311G* reoptimized geometry. [c] Experimental X-ray geometry **C** (see Table 1).

In addition, the calculated BLYP/6-311G* zero-field splitting parameter D is found for $^5[\mathbf{3}]^0$ to be negative (−1.6 cm^{-1}), but the experimentally found value of the D parameter is positive, and the finite $\lvert E/D \rvert$ ratio of 0.21 is inconsistent with the experimentally assumed value (0.07). First of all, the choice of a nonhybrid functional for zero-field splitting calculations should not affect the sign and/or magnitude of the calculated D values in comparison to hybrid functionals such as B3LYP, although their performance is reported to be worse.[27c] The CASSCF approach is reported to yield results more consistently in agreement with experimental values than DFT, so we employ it

DOI: 10.1021/acs.inorgchem.5b00229
Inorg. Chem. 2015, 54, 5691−5706

for $^5[\mathbf{3}]^0$ and $^4[\mathbf{3}]^+$. Essentially, the CASSCF calculations yield more negative values of D than DFT, concluding that DFT underestimates the magnitude of D by approximately 50%. The state averaged CASSCF calculations of $^5[\mathbf{3}]^0$, which used 5 quintet configurations and 35 triplet configurations (accounting only for the SOC contributions), yield a negative value of the D parameter of -2.84 cm^{-1}. A minimal space MRCI calculation allows inclusion of spin−spin coupling (SSC) contributions as well, which yields a total $D = -3.32$ cm^{-1}. Thus, the SSC contribution is roughly 10% of the total D value. Finally, the CASSCF E/D ratios of $^5[\mathbf{3}]^0$ are found around 0.2, irrespective of the accounted number of quintet/triplet states and dynamic electron correlation, which is also in good agreement with the DFT calculation of $^5[\mathbf{3}]^0$. Thus, the sign of the D parameter is identified to be negative when considering the theoretical results for the B3LYP/6-311G* optimized geometry. However, the complex and coordination geometry in the DCM−toluene glass measurement does not have to be consistent with the reoptimized and/or freely relaxed structure. Hence, an additional series of BLYP and CASSCF(4,5) calculations has been performed for the experimental **C** geometry (see Table 1). In comparison to the theoretical geometry, which is more likely a square pyramid, experimental geometry **C** closely resembles axially compressed pseudo-octahedral coordination. Usage of the experimental geometry **C** lead to a positive D parameter at both DFT and CASSCF(4,5) levels, with the latter method giving $D = +3.546$ cm^{-1}. Agreement with the experimental E/D ratio is also better when using the experimental geometry C. The effects of static correlation and/or the SSC and SOC contributions remain the same irrespective of the geometry used, but the sign of the D parameter is completely controlled by the coordination mode of the central atom. In this respect, systematic studies to find the best method to predict the zero-field splitting of a Mn(III) complexes have been published.[27c] The only previous, well-documented cases of positive D for six-coordinate Mn(III) with light atom (N,O) in coordination polyhedra are [Mn(bpea)(N_3)$_3$] (where bpea = *N*,*N*-bis(2-pyridylmethyl)-ethylamine)[67] and [Mn(bpia)(OAc)(OCH_3)](PF_6) (where bpia is bis(picolyl)(*N*-methylimidazole-2-yl)amine).[68] In these complexes, the zero-field splitting parameters are the following, respectively: $D = +3.50(1)$ cm^{-1}, $E = 0.82(1)$ cm^{-1}, and $D = +3.526(3)$ cm^{-1}, $E = 0.588(6)$ cm^{-1}. Thus, in the first case, $|E/D| = 0.23$, and, in the second, $|E/D| = 0.167$, values which are both (to one significant figure) in the "danger zone", and are thus very different from the unambiguously positive D (i.e., uniaxial) values found in typical (elongated) Mn(III) complexes. Nevertheless, in both of these previous cases, the complexes are described as compressed, e.g., "The complex is of particular interest given the biochemical activity and the unusual stereochemistry distinguished by a rare example of a tetragonally compressed octahedron and a pronounced angular distortion imposed by the tetradentate tripodal bpia ligand."[68] Cicera et al.[69] have shown that the change in sign of the D parameter is controlled by axial elongation and compression in the Jahn−Teller distorted hexacoordinate $[\mathrm{Mn^{III}Cl_6}]^{3-}$ complexes.

For $^4[\mathbf{3}]^+$ (theoretically optimized geometry) the D parameter is found to be about 3 times smaller than that in the case of $^5[\mathbf{3}]^0$, see Table 4. E/D ratio is less sensitive to static electron correlation when comparing the BLYP and CAS results, and the static correlation adds about 20% to the D parameter when all states are averaged for the quartet and doublet states, see Table 4.

Conclusion. Nickel(II)-, copper(II)-, and manganese(III)-salen type Schiff base complexes bearing a disiloxane moiety **1**−**3** have been prepared and characterized by spectroscopic and X-ray diffraction methods. In contrast to numerous examples reported on salen-type transition metal complexes,[9] in which the tetradentate ligand adopts a *cis*-arrangement of donor atoms around central metal ion, a *trans*-configuration was found in **1**−**3**, and in complexes **4**−**6** previously reported by us.[11] Upon oxidation of **1** and **2**, two reversible or nearly reversible anodic oxidation processes take place. In stark contrast to **1** and **2**, the oxidation of **3** is irreversible. The spectroelectrochemical experiment performed for nickel(II) complex **1** coupled with EPR measurements at 130 K confirmed the formation of [Ni(II/III)L]$^+$ species with strong noninnocent character exhibiting a rhombic EPR signal with a large g-tensor anisotropy ($g_1 = 2.1329$, $g_2 = 2.0553$, and $g_3 = 2.0183$) and intense NIR band at 1894 nm upon the first oxidation step. For copper complex **2**, the absorption at 1352 nm for the $[\mathbf{2}]^+$ cation corresponds to the α,β-HOMO to α,β-LUMO transition, with dominating charge transfer from the phenolic groups to the central atom and [MN_2O_2] coordination polyhedron having a very similar character to the NIR band of $[\mathbf{1}]^+$ mentioned above.

Following the B3LYP/6-311G* analysis of the localized orbitals it can be concluded that Ni is the redox active site in the first step of oxidation of **1**, leading to a Ni(II)/Ni(III) intermediate with the ratio 3/1, with nickel having a $3d^{7.75}$ population. In the second oxidation step, the ligand becomes oxidized, and the formal electronic d^8 configuration, Ni(II), is restored. In the case of **2**, the ligand is initially oxidized, and copper remains in the d^9 configuration, Cu(II), during both oxidation steps. Finally, for **3**, the Mn(III) ion becomes oxidized to Mn(IV). These results can be related to the shape of the respective HOMOs, which indicate the oxidation site (ligand vs central atom) for a given complex.

HFEPR investigation of **3** showed that its zero-field splitting was positive ($D > 0$) which is highly unusual for a Mn(III) coordination complex with N,O donors. Mn(III) with such a coordination sphere has been extensively investigated by HFEPR, and these complexes generally exhibit $D < 0$.[43,45,58,60,67,70−72] This finding was correlated with the structural evidence for axial compression in agreement with simple ligand-field theory. This positive D value has been confirmed by DFT/CASSCF(4,5) calculations on the experimental geometry **C**, while the reoptimized structure, which has to be considered as a square pyramid, yields a negative D value at both DFT and CASSCF(4,5) levels of theory.

■ ASSOCIATED CONTENT

Ⓢ Supporting Information

Cyclic voltammograms of complexes **1**−**6** (Figures S1 and S2); UV−vis−NIR spectra of **1**−**3** in CH_2Cl_2 (Figure S3); molecular orbitals predominantly contributing to the lowest electronic transitions for $^1[\mathbf{1}]^0$ (Figure S4), $^2[\mathbf{2}]^0$ (Figure S5), and $^5[\mathbf{3}]^0$ (Figure S6); experimental and simulated HFEPR spectra of **3** (Figure S7); crystallographic data and details of data collection and refinement for $\mathbf{1}\cdot 0.5CH_2Cl_2$, $\mathbf{2}\cdot 1.5H_2O$, and $\mathbf{3}\cdot 0.15H_2O$ (Table S1); selected bond lengths (Å) and bond angles (deg) in X-ray diffraction structures of **1**−**3** (Table S2); DFT energies and free energies of the optimized structures studied in this work (Table S3); selected bond lengths (Å) and bond angles (deg) of [**1**]^0, [**2**]^0, and [**3**]^0 resulting from DFT geometry optimizations (Table S4); calculated EPR parameters at B3LYP and BLYP levels of theory (Table S5). Crystallographic data in CIF format. The Supporting Information is available free of charge on the ACS Publications website at DOI: 10.1021/acs.inorgchem.5b00229.

AUTHOR INFORMATION

Corresponding Authors

*E-mail: shova@icmpp.ro.
*E-mail: peter.rapta@stuba.sk.
*E-mail: vladimir.arion@univie.ac.at.

Notes

The authors declare no competing financial interest.

ACKNOWLEDGMENTS

This work was supported by grants of the Romanian Ministry of National Education, CNCS−UEFISCDI, project numbers PN-II-ID-PCE-2012-4-0261 (Contract 53/2013) and PN-II-CT-RO-AT-2013-1 (Contract 749/2014). We acknowledge the financial support of the Austrian Agency for International Cooperation in Education and Research (OEAD) (grant nos. SK02/2013 and RO01/2014). This work was supported by the Science and Technology Assistance Agency under the contract no. APVV-0202-10 and by the Slovak Grant Agency VEGA under the contract nos. 1/0327/12 and 1/0307/14. We thank the HPC center at the Slovak University of Technology in Bratislava, which is a part of the Slovak Infrastructure of High Performance Computing (SIVVP Project No. 26230120002, funded by the European Region Development Funds), for computing facilities. Part of this work was done at the NHMFL, Tallahassee, FL, which is funded by NSF (Cooperative Agreement DMR 1157490), the State of Florida, and the US Department of Energy.

REFERENCES

(1) Asami, K.; Tsukidate, K.; Iwatsuki, S.; Tani, F.; Karasawa, S.; Chiang, L.; Storr, T.; Thomas, F.; Shimazaki, Y. *Inorg. Chem.* **2012**, *51*, 12450−12461.

(2) (a) Chiric, P. J.; Wieghardt, K. *Science* **2010**, *327*, 794−795. (b) Holland, P. L. *Acc. Chem. Res.* **2008**, *41*, 905−914. (c) de Bruin, B.; Hetterscheid, D. G. H.; Koekkoek, A. J. J.; Grützmacher, H. *Prog. Inorg. Chem.* **2007**, *55*, 247−253.

(3) (a) Chaudhuri, P.; Verani, C. N.; Bill, E.; Bothe, E.; Weyhermüller, T.; Wieghardt, K. *J. Am. Chem. Soc.* **2001**, *123*, 2213−2223. (b) Herebian, D.; Bothe, E.; Bill, E.; Weyhermüller, T.; Wieghardt, K. *J. Am. Chem. Soc.* **2001**, *123*, 10012−10023.

(4) (a) Shimazaki, Y.; Tani, F.; Fukui, K.; Naruta, Y.; Yamauchi, O. *J. Am. Chem. Soc.* **2003**, *125*, 10512−10513. (b) Shimazaki, Y.; Yajima, T.; Tani, F.; Karasawa, S.; Fukui, K.; Naruta, Y.; Yamauchi, O. *J. Am. Chem. Soc.* **2007**, *129*, 2559−2568. (c) Shimazaki, Y.; Arai, N.; Dunn, T.; Yajima, T.; Tani, F.; Ramogida, C. F.; Storr, T. *Dalton Trans.* **2011**, *40*, 2469−2479.

(5) (a) Rotthaus, O.; Jarjayes, O.; Thomas, F.; Philouze, C.; Del Valle, C. P.; Saint-Aman, E.; Pierre, J.-L. *Chem.—Eur. J.* **2006**, *12*, 2293−2302. (b) Rotthaus, O.; Thomas, F.; Jarjayes, O.; Philouze, C.; Saint-Aman, E.; Pierre, J.-L. *Chem.—Eur. J.* **2006**, *12*, 6953−6962. (c) Chiang, L.; Kochem, A.; Jarjayes, O.; Dunn, T. J.; Vezin, H.; Sakaguchi, M.; Ogura, T.; Orio, M.; Shimazaki, Y.; Thomas, F.; Storr, T. *Chem.—Eur. J.* **2012**, *18*, 14117−14127.

(6) (a) Storr, T.; Wasinger, E. C.; Pratt, R. C.; Stack, T. D. P. *Angew. Chem., Int. Ed.* **2007**, *46*, 5198−5201. (b) Storr, T.; Verma, P.; Shimazaki, Y.; Wasinger, E. C.; Stack, T. D. P. *Chem.—Eur. J.* **2010**, *16*, 8980−8983.

(7) Storr, T.; Verma, P.; Pratt, R. C.; Wasinger, E. C.; Shimazaki, Y.; Stack, T. D. P. *J. Am. Chem. Soc.* **2008**, *130*, 15448−15459.

(8) Arion, V. B.; Rapta, P.; Telser, J.; Shova, S. S.; Breza, M.; Lušpai, K.; Kožišek, J. *Inorg. Chem.* **2011**, *50*, 2918−2931.

(9) (a) Goldberg, D. P.; Lippard, S. J. *Adv. Chem. Ser.* **1995**, *246*, 61−81. (b) Chaudhuri, P.; Wieghardt, K. *Prog. Inorg. Chem.* **2001**, *50*, 151−216. (c) Jazdzewski, B. A.; Tolman, W. B. *Coord. Chem. Rev.* **2000**, *200−202*, 633−685. (d) Itoh, S.; Taki, M.; Fukuzumi, S. *Coord. Chem. Rev.* **2000**, *198*, 3−20. (e) Saint-Aman, E.; Ménage, S.; Pierre, J.-L.; Defrancq, E.; Gellon, G. *New J. Chem.* **1998**, 393−394. (f) Pratt, R. C.; Stack, T. D. P. *Inorg. Chem.* **2005**, *44*, 2367−2375. (g) Nairn, A. K.; Archibald, S. J.; Bhalla, R.; Gilbert, B. C.; MacLean, E. J.; Teat, S. J.; Walton, P. H. *Dalton Trans.* **2006**, 172−176. (h) Bernardo, K.; Leppard, S.; Robert, A.; Commenges, G.; Fahan, F.; Meunier, B. *Inorg. Chem.* **1996**, *35*, 387−396. (i) Bill, E.; Müller, J.; Weyhermüller, T.; Wieghardt, K. *Inorg. Chem.* **1999**, *38*, 5795−5802.

(10) (a) Yao, H. H.; Lo, J. M.; Chen, B. H.; Lu, T. H. *Acta Crystallogr., Sect. C: Cryst. Struct. Commun.* **1997**, *53*, 1012−1013. (b) Wang, Y. D.; DuBois, J. I.; Hedman, B.; Hodgson, K. O.; Stack, T. D. P. *Science* **1998**, *279*, 537−540.

(11) Soroceanu, A.; Cazacu, M.; Shova, S.; Turta, C.; Kožíšek, J.; Gall, M.; Breza, M.; Rapta, P.; Mac Leod, T. C. O.; Pombeiro, A. J. L.; Telser, J.; Dobrov, A. A.; Arion, V. B. *Eur. J. Inorg. Chem.* **2013**, 1458−1474.

(12) *CrysAlis RED, Version 1.171.36.32*; Oxford Diffraction Ltd., 2003.

(13) OLEX2: a complete structure solution, refinement and analysis program: Dolomanov, O. V.; Bourhis, L. J.; Gildea, R. J.; Howard, J. A. K.; Puschmann, H. *J. Appl. Crystallogr.* **2009**, *42*, 339−341.

(14) Sheldrick, G. M. *Acta Crystallogr.* **2008**, *A64*, 112−122.

(15) Hassan, A. K.; Pardi, L. A.; Krzystek, J.; Sienkiewicz, A.; Goy, P.; Rohrer, M.; Brunel, L.-C. *J. Magn. Reson.* **2000**, *142*, 300−312.

(16) (a) Lee, C.; Yang, W.; Parr, R. G. *Phys. Rev. B* **1988**, *37*, 785−789. (b) Becke, A. D. *J. Chem. Phys.* **1993**, *98*, 5648−5651.

(17) (a) Stephens, P. J.; Devlin, F. J.; Chabalowski, C. F.; Frisch, M. J. *J. Phys. Chem.* **1994**, *98*, 11623−11627. (b) Vosko, S. H.; Wilk, L.; Nusair, M. *Can. J. Phys.* **1980**, *58*, 1200−1211.

(18) Frisch, M. J.; et al. *Gaussian 03, Revision D.01*; Gaussian, Inc.: Wallingford, CT, 2004; www.gaussian.com.

(19) (a) Krishnan, R.; Binkley, J. S.; Seeger, R.; Pople, J. A. *J. Chem. Phys.* **1980**, *72*, 650−654. (b) McLean, A. D.; Chandler, G. S. *J. Chem. Phys.* **1980**, *72*, 5639−5648. (c) Wachters, A. J. H. *J. Chem. Phys.* **1970**, *52*, 1033−1036.

(20) (a) Carpenter, J. E.; Weinhold, F. *THEOCHEM* **1988**, *169*, 41−62. (b) Reed, A. E.; Curtiss, L. A.; Weinhold, F. *Chem. Rev.* **1988**, *88*, 899−926.

(21) Bachler, V.; Olbrich, G.; Neese, F.; Wieghardt, K. *Inorg. Chem.* **2002**, *42*, 4179−4193.

(22) Yamaguchi, K.; Tsunekawa, T.; Toyoda, Y.; Fueno, T. *Chem. Phys. Lett.* **1988**, *143*, 371−376.

(23) ORCA program system: Neese, F. *Wiley Interdiscip. Rev.: Comput. Mol. Sci.* **2012**, *2*, 73−78.

(24) Pipek, J.; Mezey, P. G. *J. Chem. Phys.* **1989**, *90*, 4916−4926.

(25) (a) Neese, F. *J. Chem. Phys.* **2001**, *115*, 11080−11096. (b) Sandhoefer, B.; Neese, F. *J. Chem. Phys.* **2012**, *137*, 094102.

(26) (a) Neese, F. *J. Chem. Phys.* **2003**, *117*, 3939−3948. (b) Koβmann, S.; Kirchner, B.; Neese, F. *Mol. Phys.* **2007**, *105*, 2049−2071.

(27) (a) Neese, F. *J. Am. Chem. Soc.* **2006**, *128*, 10213−10222. (b) Neese, F. *J. Chem. Phys.* **2007**, *127*, 164112. (c) Duboc, C.; Ganyushin, D.; Sivalingam, K.; Collomb, M. N.; Neese, F. *J. Phys. Chem. A* **2010**, *114*, 10750−10758.

(28) Sinnecker, S.; Rajendran, A.; Klamt, A.; Diedenhofen, M.; Neese, F. *J. Phys. Chem. A* **2006**, *110*, 2235−2245.

(29) (a) Jayatilaka, D.; Grimwood, D.J. *Tonto: A Research Tool for Quantum Chemistry*; The University of Western Australia: Nedlands, Western Australia, Australia, 2000; http://www.theochem.uwa.edu.au. (b) Jayatilaka, D.; Grimwood, D. J. *Computational Science—ICCS 4*; Springer: Berlin, 2003; p 142.

(30) Zein, S.; Neese. *J. Phys. Chem. A* **2008**, *112*, 7976−7983.

(31) Romain, S.; Duboc, C.; Neese, F.; Riviere, E.; Hanton, L. R.; Blackman, A. G.; Philouze, C.; Lepretre, J.-C.; Deronzier, A.; Collomb, M.-N. *Chem.—Eur. J.* **2009**, *15*, 980−988.

(32) Yang, L.; Powell, D. R.; Houser, R. P. *Dalton Trans.* **2007**, 955−964.

(33) (a) Bonadies, J. A.; Kirk, M. L.; Soo Lah, M.; Kessissoglou, D. P.; Hatfield, W. E.; Pecoraro, V. L. *Inorg. Chem.* **1989**, *28*, 2037−2044. (b) Martinez, D.; Motevalli, M.; Watkinson, M. *Dalton Trans.* **2010**, *39*, 446−455.

(34) (a) Watkinson, M.; Fondo, M.; Bermejo, M. R.; Sousa, A.; McAuliffe, C. A.; Pritchard, R. G.; Jaiboon, N.; Aurangzeb, N.; Naeem, M. *Dalton Trans.* **1999**, 31−41. (b) Ha, K. *Z. Kristallogr.—New Cryst. Struct.* **2010**, *225*, 257−258.

(35) Asada, H.; Fujiwara, M.; Matsushita, T. *Polyhedron* **2000**, *19*, 2039−2048.

(36) (a) Gennari, M.; Orio, M.; Pécaut, J.; Bothe, E.; Neese, F.; Collomb, M.-N.; Duboc, C. *Inorg. Chem.* **2011**, *50*, 3707−3716. (b) Cao, T.-P.-A.; Nocton, G.; Ricard, L.; Le Goff, X. F.; Auffrant, A. *Angew. Chem., Int. Ed.* **2014**, *53*, 1368−1372. (c) Lappin, A. G.; McAuley, A. *Adv. Inorg. Chem.* **1988**, *32*, 241−295.

(37) Arion, V. B.; Platzer, S.; Rapta, P.; Machata, P.; Breza, M.; Vegh, D.; Dunsch, L.; Telser, J.; Shova, S.; Mac Leod, T. C. O.; Pombeiro, A. J. L. *Inorg. Chem.* **2013**, *52*, 7524−7540.

(38) Machata, P.; Herich, P.; Lušpai, K.; Bučinský, L.; Šoralová, S.; Breza, M.; Kožíšek, J.; Rapta, P. *Organometallics* **2014**, *33*, 4846−4859.

(39) Herich, P.; Fronc, M.; Kožíšek, J. *Acta Crystallogr.* **2015**, *C71*, 159−164.

(40) Broering, E. P.; Dillon, S.; Gale, E. M.; Steiner, R. A.; Telser, J.; Brunold, T. C.; Harrop, T. C. *Inorg. Chem.* **2015**, *54*, 3815−3828.

(41) (a) Lyons, C. T.; Stack, D. P. *Coord. Chem. Rev.* **2013**, *257*, 528−540. (b) Shimazaki, Y. Oxidation Chemistry of Metal(II) Salen-Type Complexes. In *Electrochemistry*; Khalid, M. A. A., Ed.; InTech: Rijeka, Croatia, 2013; Chapter 3, pp 51−70.

(42) Krivokapic, I.; Noble, C.; Klitgaard, S.; Tregenna-Piggott, P. L. W.; Weihe, H.; Barra, A.-L. *Angew. Chem., Int. Ed.* **2005**, *44*, 3613−3616.

(43) Aromí, G.; Telser, J.; Ozarowski, A.; Brunel, L.-C.; Stoeckli-Evans, H.-M.; Krzystek, J. *Inorg. Chem.* **2005**, *44*, 187−196.

(44) Krzystek, J.; Zvyagin, S. A.; Ozarowski, A.; Trofimenko, S.; Telser, J. *J. Magn. Reson.* **2006**, *178*, 174−183.

(45) Hendrich, M. P.; Debrunner, P. G. *Biophys. J.* **1989**, *56*, 489−506.

(46) Dexheimer, S. L.; Gohdes, J. W.; Chan, M. K.; Hagen, K. S.; Armstrong, W. H.; Klein, M. P. *J. Am. Chem. Soc.* **1989**, *111*, 8923−8925.

(47) Campbell, K. A.; Yikilmaz, E.; Grant, C. V.; Gregor, W.; Miller, A.-F.; Britt, R. D. *J. Am. Chem. Soc.* **1999**, *121*, 4714−4715.

(48) Britt, R. D.; Peloquin, J. M.; Campbell, K. A. *Annu. Rev. Biophys. Biomol. Struct.* **2000**, *29*, 463−495.

(49) Campbell, K. A.; Force, D. A.; Nixon, P. J.; Dole, F.; Diner, B. A.; Britt, R. D. *J. Am. Chem. Soc.* **2000**, *122*, 3754−3761.

(50) Campbell, K. A.; Lashley, M. R.; Wyatt, J. K.; Nantz, M. H.; Britt, R. D. *J. Am. Chem. Soc.* **2001**, *123*, 5710−5719.

(51) Krzystek, J.; Yeagle, G.; Park, J.-H.; Meisel, M. W.; Britt, R. D.; Brunel, L.-C.; Telser, J. *Inorg. Chem.* **2003**, *42*, 4610−4618; Correction: *Inorg. Chem.* **2009**, *48*, 3290.

(52) Grigoropoulos, A.; Pissas, M.; Papatolis, P.; Psycharis, V.; Kyritsis, P.; Sanakis, Y. *Inorg. Chem.* **2013**, *52*, 12869−12871.

(53) Gupta, R.; Taguchi, T.; Borovik, A. S.; Hendrich, M. P. *Inorg. Chem.* **2013**, *52*, 12568−12575.

(54) Birk, T.; Pedersen, K. S.; Piligkos, S.; Thuesen, C. A.; Weihe, H.; Bendix, J. *Inorg. Chem.* **2011**, *50*, 5312−5314.

(55) Scheifele, Q.; Birk, T.; Bendix, J.; Tregenna-Piggot; Weihe, H. *Angew. Chem., Int. Ed.* **2007**, *47*, 148−150.

(56) Talsi, E. P.; Bryliakov, K. P. *Mendeleev Commun.* **2004**, *14*, 111−112.

(57) Telser, J.; Ozarowski, A.; Krzystek, J. High-frequency and -field electron paramagnetic resonance of transition metal ion (d block) coordination complexes. In *Electron Paramagnetic Resonance*; The Royal Society of Chemistry: London, U.K., 2013; Vol. *23*, pp 209−263.

(58) Telser, J.; Krzystek, J.; Ozarowski, A. *J. Biol. Inorg. Chem.* **2014**, *19*, 297−318.

(59) Mossin, S.; Weihe, H.; Barra, A.-L. *J. Am. Chem. Soc.* **2002**, *124*, 8764−8765.

(60) Krzystek, J.; Telser, J. *J. Magn. Reson.* **2003**, *162*, 454−465.

(61) Carver, G.; Thut, M.; Noble, C.; Tregenna-Piggott, P. L. W. *J. Chem. Theory Comput.* **2008**, *4*, 603−613.

(62) Tregenna-Piggott, P. L. W. *Inorg. Chem.* **2008**, *47*, 448−453.

(63) (a) Radoń, M. *Phys. Chem. Chem. Phys.* **2014**, *16*, 14479−14488. (b) Harvey, J. N. *Annu. Rep. Prog. Chem., Sect. C: Phys. Chem.* **2006**, *102*, 203−226. (c) Ghosh, A. *J. Biol. Inorg. Chem.* **2006**, *11*, 712−724. (d) Conradie, J.; Ghosh, A. *J. Phys. Chem. B* **2007**, *111*, 12621−12624. (e) Harvey, J. N. *Struct. Bonding (Berlin)* **2004**, *112*, 151−183. (f) Reiher, M.; Salomon, O.; Hess, B. A. *Theor. Chem. Acc.* **2001**, *107*, 48−55. (g) Salomon, O.; Reiher, M.; Hess, B. A. *J. Chem. Phys.* **2002**, *117*, 4729−4737. (h) Swart, M. *Inorg. Chim. Acta* **2007**, *360*, 179−189. (i) Swart, M. *J. Chem. Theory Comput.* **2008**, *4*, 2057−2066. (j) Stephens; Devlin, F. J.; Chabalowski, C. F.; Frisch, M. J. *J. Phys. Chem.* **1994**, *98*, 11623−11627. (l) Ganzenmüller, G.; Berkaïne, N.; Fouqueau, A.; Casida, M. E.; Reiher, M. *J. Chem. Phys.* **2005**, *122*, 234321.

(64) Bučinský, L.; Büchel, G. E.; Ponec, R.; Rapta, P.; Breza, M.; Kožíšek, J.; Gall, M.; Biskupič, S.; Fronc, M.; Schiessl, K.; Cuzan, O.; Prodius, D.; Turta, C.; Shova, S.; Zając, D. A.; Arion, V. B. *Eur. J. Inorg. Chem.* **2013**, 2505−2519.

(65) (a) Noodleman, L. *J. Chem. Phys.* **1981**, *74*, 5737−5743. (b) Noodleman, L.; Davidson, E. R. *Chem. Phys.* **1986**, *109*, 131−143. (c) Ovchinnikov, A. A.; Labanowski, J. K. *Phys. Rev. A* **1996**, *53*, 3946−3952. (d) Adamo, C.; Barone, V.; Bencini, A.; Totti, F.; Ciofini, I. *Inorg. Chem.* **1999**, *38*, 1996−2004.

(66) Supporting Information Table S5 shows the influence of the choice of BLYP vs B3LYP functional as well as COSMO solvent effects and/or the sensitivity to the inclusion of diffuse functions on the obtained values of *g*-tensor, zero-field splitting *E*/*D* values, and hyperfine coupling constants of the studied compounds.

(67) Mantel, C.; Hassan, A. K.; Pécaut, J.; Deronzier, A.; Collomb, M.-N.; Duboc-Toia, C. *J. Am. Chem. Soc.* **2003**, *125*, 12337−12344.

(68) Scheifele, Q.; Riplinger, C.; Neese, F.; Weihe, H.; Barra, A.-L.; Juranyi, F.; Podlesnyak, A.; Tregenna-Piggott, P. L. W. *Inorg. Chem.* **2008**, *47*, 439−447.

(69) Cicera, J.; Ruiz, E.; Alvarez, S.; Neese, F.; Kortus, J. *Chem.—Eur. J.* **2009**, *15*, 4078−4087.

(70) Limburg, J.; Vrettos, J. S.; Crabtree, R. H.; Brudvig, G. W.; de Paula, J. C.; Hassan, A.; Barra, A.-L.; Duboc-Toia, C.; Collomb, M.-N. *Inorg. Chem.* **2001**, *40*, 1698−1703.

(71) Krzystek, J.; Telser, J.; Knapp, M. J.; Hendrickson, D. N.; Aromí, G.; Christou, G.; Angerhofer, A.; Brunel, L.-C. *Appl. Magn. Reson.* **2001**, *23*, 571−585.

(72) Krzystek, J.; Ozarowski, A.; Telser, J. *Coord. Chem. Rev.* **2006**, *250*, 2308−2324.